Objective Image Segmentation Method for Morphological Features in Spiral Galaxies

(近傍渦巻銀河画像における形態学的特徴の客観的な分割手法)

Observational Astronomy Laboratory,
Department of Cosmosciences,
Graduate School of Science, Hokkaido University
Kazuki SHIMIZU

March 2025

Abstract

Morphological features of a spiral galaxy (e.g., spiral arm or bar) are directly related to star formation since the morphology of a galaxy is just the distribution of stars. The morphology is also related to the amount and dynamics (density, temperature, velocity, etc.) of gas, which is the raw material of stars, and motions of stars over long time periods. Therefore, it is important to consider physical properties for each morphological feature of a galaxy. However, an general, objective standard to segment an image into morphological features has not been established yet. At present, many studies performed image segmentation by visual inspection. Hence, it is difficult to quantitatively compare and discuss the results of previous studies. In this study, we aimed to establish a method to segment a galaxy image into its morphological features.

This study makes the following two assumptions: 1) A steep change in color corresponding to an intensity change are recognized as the border of a morphological feature. 2) The intensity of a galaxy is a superposition of low- and high-spatial-frequency components (hereafter global and local components). Global components extend throughout the galaxy and can be represented by such as Sérsic's law, while local components are visually regarded as morphological features. Under the assumptions, we separate these two components from the original intensity map without a specific mathematical model in order to treat with a galaxy even if it has distorted morphology. In addition, we determine the sizes of morphological features (e.g., width of spiral arm) for each pixel since it change within the galaxy. Filtering methods by spatial frequency widely used today, such as the Fourier transform, cannot handle arbitrary multiple scales in a single image.

First, we extract local components when morphological features have a fixed scale D. For each pixel P in the map, neighboring pixels from the pixel P within D are selected. In other words, we select a circular range within a distance $D/2$ from the pixel P. We expand the two-dimensional image to surface plots of three-dimensional space (x, y, z). The value of z direction is an intensity at each pixel. In each surface plot of the circular region, we select three points satisfying the following conditions: 1) minimum intensity point A; 2) point B, where the angle

between line segment AB and the x-y plane is minimum; 3) point C, where the angle between the x-y plane and the plane that includes ΔABC is minimum. In other words, ΔABC is the triangle with the lowest intensity and the smallest angle between the xy plane within the circular region. If the pixel P is at the center of morphological features, the triangle ΔABC is located at a border of local and global components at the pixel P in three-dimensional space. This is because the plane with the lowest intensity and the smallest angle between the xy plane is defined by the three points outside morphological features if a width of the features is smaller than D. Therefore, the local components can be extracted if a size of morphological features is D.

Next, we determine an accurate spatial scale for each pixel. Assume that P is located at the center of a morphological feature and its width is D_a. The intensity of the global components at the pixel P changes its trend around D_a for increasing D. When D is smaller than D_a, the intensities of the plane become higher than the accurate boundary of global and local components since not all pixels of the morphological feature are included within the region. When D is larger than D_a, and a local minimum pixel is included the circular region with radios D, the same boundary as that of D_a should be determined. Hence, we determine an accurate spatial scale, and obtain local component map using accurate scales D_a for each pixel.

The local component map can be easily identified morphological feature pixels, and non-feature pixels can be distinguished by a single threshold. Some point sources are emphasized and remain in the masked map. These are removed by combining established image processing method such as friend-of-friend algorithm.

Finally, a central region is labeled as bar-like region. This region is a bar of SAB and SB galaxies or a spatially unresolved inner arm of SA galaxies.

To investigate molecular gas and star formation distribution among various morphological features, we targeted 147 galaxies listed in the legacy project CO Multi-line Imaging of Nearby Galaxies (COMING), which was conducted with the 45-m telescope at the Nobeyama Radio Observatory. More than half of the galaxies are not able to be applied our method due to small apparent sizes. Most of the rest galaxies with relative large apparent sizes can be emphasized these morphological features correctly. However, a bar-like region may not be determined correctly for galaxies with relative small apparent sizes. Our method typically works well for galaxies with a spatial resolution finer than about 0.17 kpc and correctly determines these morphological features of 17 galaxies. For these 17 galaxies, we investigated the relation between star formation rate (SFR) surface density and molecular gas mass surface density. Higher SFR per molecular gas mass (star formation efficiency) value is found for SB galaxies in the COMING samples.

Contents

1 Introduction

Many physical properties of a galaxy can be determined from its morphology. The morphological features are directly related to star formation since the morphology of a galaxy is just the distribution of its stars (Kennicutt 1983, 1996). Therefore, morphology is also related to the amount and dynamics of gas, which is the raw material of stars (Egusa et al. 2017; Yamamoto et al. 2018), the dynamics and stability of stars (Sánchez-Martín et al. 2023; Iles et al. 2022), and metallicity, which is associated with star formation (Tremonti et al. 2004; Moustakas et al. 2010). The abundance of gas inflow from outside a galaxy, which is strongly influenced by the galactic environment, has a significant impact on star formation. Consequently, galaxy morphology is related to differences in star formation in different galactic environments (Gunn & Gott 1972; Dressler 1980), as well as galaxy evolution (Leśniewska et al. 2023; Alfonzo et al. 2024).

The pixel-by-pixel relation between the star formation rate (SFR) and molecular gas amount has been studied. Momose et al. (2010) visually determined the bar, spiral arm, inter-arm, and center regions of NGC 4303 to investigate their relationship. Yajima et al. (2020) studied the pixel-by-pixel definition of morphological features and the relation between star formation efficiency (SFE) and molecular gas mass for three galaxies, namely NGC 2903, NGC 3627, and NGC 4303. They found that SFE decreases in regions with large velocity dispersion for the three galaxies. Since it seems that morphology is related to star formation in this way, it is important to establish accurate feature determination for confirmation of the difference in physical properties among morphological features.

1.1 Morphological features of galaxies

Many studies have classified galaxies based on the relationship between their physical properties and morphology. Hubble (1926) published a classification of galaxies according to their morphological features (e.g., elliptical or spiral, presence of bar at galaxy center, tight or loose pitch angles of arms). The Hubble classification and its tuning-fork diagram are still widely used today because they are simple and effective. De Vaucouleur (1959) extended the Hubble classification by subdividing each Hubble class and adding a class for arms near the center (e.g., ring (r) and spiral (s)). Many morphological classifications that focus on specific features have been published, such as the Yerkes classification (Morgan et al. 1957), Revised David Dunlap Observatory classification (van den Bergh 1976), box-shaped/disk-shaped classification for elliptical galaxies or bulge of spiral galaxies (Bender et al. 1988), and classification of radio galaxies (Fanaroff et al. 1974). Classifications limited to spiral arms include grand-design/flocculent galaxies (Elmegreen & Elmegreen 1982) and the arm class (Elmegreen & Elmegreen 1987).

However, these classifications are subjective as they depend on visual inspection. Danver (1942) compared the morphological classification of galaxies in several studies and pointed out that the differences in classification are large, especially for flocculent galaxies. De Vaucouleur (1959) found a large dispersion of results obtained using visual classification and highlighted the importance of objective classification criteria. Naim et al. (1995) conducted a classification of 831 galaxies by six people according to the Hubble classification and found a large dispersion. Galaxy Zoo (Raddick et al. 2007) is a scientific project that invites members of the public to help classify galaxies; the large number of participants increases accuracy.

Some nonparametric methods have been developed. Abraham et al. (1994, 1996) and Conselice et al. (2000a) introduced concentration index C to discuss the bulge/disk ratio of spiral galaxies. Schade et al. (1995) and Bershady et al. (2000) introduced rotational asymmetry A to classify early and late Hubble-type galaxies and detect merging and irregular galaxies. Conselice (2003) introduced clumpiness parameter S and proposed the concentration, asymmetry, and clumpiness (CAS) method, which combines these parameters. Lotz & Madau (2004) applied the Gini coefficient to images of spiral galaxies. The Gini coefficient is an index that obtains the distribution bias from the area bound by the Lorentz curve of the uniform distribution and the Lorentz curve of the target. They redefined the Gini coefficient as a statistical index for measuring the distribution of flux values within an image of a galaxy and established a stable method at low resolutions.

Methods for determining the number of arms from galaxy images have also been developed. It has long been known that many spiral arms are logarithmic (Danver 1942; Lin & Shu 1964) and that spiral arms in an image can be detected by linear fitting with polar coordinate transformed images (Davis & Hayes 2014; Slater & Bell 2014). Methods for determining the number of spiral arms in a galaxy image using the Fourier transform, based on the property that spiral arms are periodic in the polar coordinate plane, have also been proposed (Kalnajs 1975; Elmegreen & Elmegreen 1984). Wozniak et al. (1995) detected a bar structure by elliptical fitting and developed a method for detecting a bar structure with an inner bar and/or a trial axis by ellipticity and position angle changes with increasing major axis length of an ellipse. In addition, a method has been proposed for detecting the existence of a bar and its properties via the Fourier transform of a polar coordinate transformed image and an intensity of $m = 2$ (Ohta et al. 1990).

The physical properties of individual morphological features have been studied on a smaller spatial scale than the whole galaxy, which is used for classification. To obtain the most accurate correlation between the morphology and physical properties of a galaxy, it is necessary to extract only the pixels that constitute a certain morphological feature from an image. As mentioned, a method for detecting and masking elliptical galaxies that have simple structures has been established. However, there is currently no pixel-by-pixel detection method for spiral galaxies that have complex internal structures. The most commonly used method for pixel-by-pixel structure detection is visual inspection. Momose et al. (2010) and Yajima et al. (2020) discussed the difference in star formation activities among morphological features and the star formation in individual morphological features (e.g., bar region, arm region). For pixel-by-pixel structure detection, morphological structures, which can be complicated and ambiguous, need to be classified. Detection by visual inspection can pick up pixels of flocculent structures, but can be subjective for galaxy type classification. To understand the extent of a certain physical property of a spiral galaxy, it is important to apply a pixel-by-pixel feature definition method with an objective standard to many galaxies. It is necessary to accurately trace the distribution of stars to obtain differences in physical properties related to morphological features. It is thus necessary to define morphological features on a pixel-by-pixel basis. Quejereta et al. (2021) made pixel-by-pixel structure images of spiral galaxies, detecting features from a ^{12}CO($J = 2 - 1$) map by visual inspection and automatically defining arm widths based on increases in intensity.

Many studies have applied deep learning, especially convolutional neural networks, to image analysis for classification and image segmentation (Bekki 2021; Tanoglidis et al. 2021; Vavilova et al. 2022; Walmsley et al. 2022). However, these studies used classifications from previous studies based on training datasets labeled using a subjective method or simulation data.

It is difficult to establish a pixel-by-pixel classification method for galaxy structures because spiral galaxies have various shapes. In addition to the shape of spiral arms, other characteristics in an image, such as the number of spiral arms, arm pitch angles, and the presence of a bar structure (if it exists, its intensity and shape), point sources scattered in the image, and interactions with other galaxies are used to define morphological features. It is very difficult to define uniform numerical criteria for all galaxies because the intensities of structures vary with galaxy.

Limitations due to galaxy location and resolution of observation data complicate the definition of morphological features. The inclinations of galactic disks significantly affect visual features. Apparent galaxy size and image resolution also have a significant impact on the detection of morphological features. In addition, since the intensity values of pixels in an intensity map are displayed as colors, the type of color map and image scale greatly affect the difficulty of detecting morphological structures. The detection of features in images that are characterized by unclear color changes (e.g., ambiguous edges, weak intensity, intermittent structures) is highly subjective.

Studies have applied image processing to enhance galaxy structures. Regan & Vogel (1994) fitted galaxy images using Sérsic's law after correcting for the inclination of the galactic disk and then subtracted the result from the image to remove the gradient of the entire galaxy to emphasize local spatial structures such as spiral arms. However, since this method is based on Sérsic's law, which is a law of radial brightness distribution, it does not work well for images whose structures distort the radial distribution, such as those with a bright, large bar. The eigenvalue of the Hesse matrix, which is the gradient in the horizontal, vertical, and diagonal directions, has been applied for galaxy filament detection (Zavagno et al. 2023) and structure extraction from our Galaxy's longitude-velocity image (Mattia et al. 2015). Starck et al. (1998) applied the wavelet transform to extract the spiral arms component of NGC 2997. In the wavelet transform, an image is regarded as a superposition of expanded and shifted small finite-size functions (called wavelets), similar to the superposition of sine functions in the Fourier transform. While the Fourier transform converts a function of position to that of spatial frequency, the wavelet transform converts a function of position to that of spatial frequency and position. For structure extraction using eigenvalues of the Hesse matrix and the wavelet transform (and the Fourier transform), the proper kernel size or wavelet size need to be selected. In addition, images with different-size structures, such as an image with a bold bar and thin spiral arms, cannot be treated.

The rest of this paper is organized as follows. In Section 2, we describe prevous methods for morphological feature detection. These methods are finally rejected, but these can be used for an appropriate image. In Section 3, we describe the proposed method in detail. We emphasize the morphological structures in an image using an approach similar to that of Regan & Vogel (1994) but without a specific model. The pixels of structures are divided into individual spiral arms and a central bar-like region (i.e., a bar structure or spiral arms that cannot be spatially resolved). In Section 4, we describe the sample galaxies. In Section 5, we present the results. In Section 6, we discuss the accuracy and effectiveness of our method based on a comparison with visual inspection and an analysis of the SFR and gas amount in arms and inter-arms. In Section 7, we give the conclusions. In addition, Some ideas and trials for arm segmentation are described in Appendix. Section 3, 5 and 6 is described in Shimizu & Sorai 2025, PASJ, under review.

2 Previous methods

All of the following methods shown in this section are performed to the galaxies observed in the project CO Multi-line Imaging of Nearby Galaxies (COMING). Galaxies, and galaxy parameters are from Sorai et al. (2019). SFR density and molecular gas density are obtained by Muraoka et al (2019).

2.1 The feature detection by relative intensity

At first, we aimed to establish the image segmentation by combining morphological feature detection and width determination of the features. Linear fitting with logarithmic polar coordinate transformed images is widely used for spiral arm detection since logarithmic spiral is linear in logarithmic polar coordinate. Fitted linearly, even intermittent arms can be detected easily. Pitch angle of spiral arm is obtained as a gradient of a line. However, a general method for determination of inner and outer edges of a spiral arm is not established. In addition, the number of spiral arms is determined in advance. In other words, the number of arms is need to be input manually. Since pixels near the galactic center are significantly expanded by transformation to logarithmic polar coordinate system, a preprocessing for linear fitting is needed such as masking. A bar structure is also need to be masked for a barred galaxy. We used the method shown in Wozniak et al. (1995) for bar masking.

Using linear fitting, we aim to detect spiral arms in an intensity map. The intensity map is transformed to logarithmic polar coordinates ($\log r - \theta$) after disk inclination correction. Before linear fitting, pixels whose locations of r-axis are smaller than semi-major axis (SMA) length of a bar is masked if a bar structure is found. If any bar is not found, pixels whose locations of r-axis are smaller than 0.05 times of the galactic radius R are masked. Next, the number of spiral arms and initial locations of each arm are determined by following method. Pixels at $r =$ SMA length or $0.05R + 0.1R$ is selected from the intensity map. If any bar is not found, $0.05R$ is used. The one-dimensional intensity map clipped by above method is masked by three times the standard deviation of the original map. After masking, pixels whose intensities are stronger than neighboring two pixels are regarded as spiral arms. We applied this method to many galaxies.

However, this method does not work well for arm number determination, since it has following problems. 1) Point sources in one-dimensional map is regarded as spiral arms. 2) Branches of arms cannot be treated with the method. Since an appropriate threshold value for masking depends on galaxies, 4) weak arms cannot be detected, and even for relative strong arms, 5) outer edges of spiral arms cannot be obtained correctly. In addition, only a little galaxies have fully logarithmic spirals. Many arms are distorted at these outer edges in logarithmic polar coordinates. This fact prevent establishing a general detection method for spiral arms of many galaxies. Therefore, the method is fixed as follows.

An image is masked inside a bar SMA length or $0.05R$ in logarithmic polar coordinates. The image is also masked by two times the standard deviation. The pixels whose intensity is stronger than the just right pixel and the just left pixel are detected and labeled as local peak pixels. Since morphological features have relative stronger intensity than surrounding pixels, local peak pixels trace spiral arms, and form curved lines. In order not to detect point sources as spiral arms, only if the curved lines are longer than $0.5R$, the traced structures are regarded as spiral arms. This detection method can treat with relative weak spiral arms and relative weak parts of arms such as outer edges. However, intermittent arms are hardly detected since these are traced as multiple short lines by local peak pixels. For some barred galaxies, an inner arm is masked if the arm extend inside SMA length, and cannot be traced by local peaks. To solve the problems, the method applied to the origiral intensity map in x–y coordinates.

A method for local peak determination is changed into following procedure in order to treat with images in x–$y$plane. The pixels whose intensity is stronger than both neighboring two pixels in x-axis direction or in y-axis direction are detected and labeled as local peak pixels. Figure 1 is an intensity map which local peak pixels are labeled in NGC 3627 in WISE 3.4 μm. Two spiral arms and a bar are traced in the figure. Cross-shaped peaks mean round, strong structures. The local peaks of the map trace not only the morphological features but noises located outside the galaxy. The local peak pixels from noises (hereinafter called noise peaks) should be removed. However, masking by three

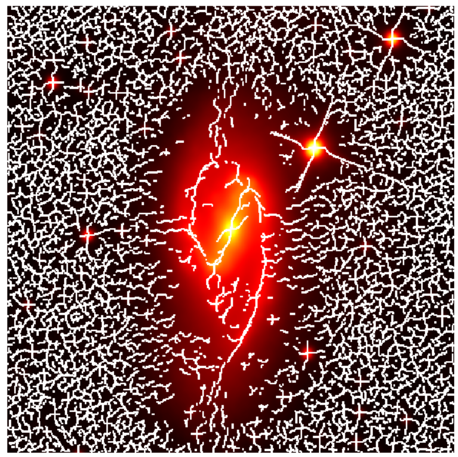

Figure 1: Peak pixels of WISE 3.4 μm maps of NGC 3627. Those are shown in white.

times standard deviation of the map or by the galactic radius cannot remove noise peaks well. Here, we focused on the property that more local peak pixels exist outside the galaxy than inside the galaxy, since noise peaks trace random distribution of noises.

The local peak density $d_{\rm local}$ is defined for each pixel to remove noise peaks.

$$d_{\rm local} = N_{\rm peak}/N_{\rm all}$$

where $N_{\rm all}$ is the number of pixels nearer than $0.2R$ from each pixel, and $N_{\rm peak}$ is the number of peak pixels in the same region. The size of the region is manually determined as an enough robust size to a noise fluctuation. The background peak density $d_{\rm out}$ is defined as an average value of $d_{\rm local}$ for pixels outside the galaxy. Whether pixels are outside the galaxy or not is determined by the galactic radius. The peak pixels whose local peak density $d_{\rm local}$ is smaller than 0.9 $d_{\rm out}$ are masked.

At the galactic center, peak pixels form a cross like point sources due to its strong intensity. The central cross may not be connected to a bar, and prevent its detection. Therefore, the bar existance is determined by the method shown in Wozniak et al. (1995). However, when a bar and roots of arms have loose connections, it is difficult for their method to determine the bar, since their method uses a drastic parameter change of ellipse fitting at the edge of the bar as SMA increases. If SMA for fitting becomes longer than the bar, a fitting ellipse cannot trace any morphological features no longer. Hence, SMA is determined where a difference of a position angle of peak pixels at the bar and that of ellipse fitting becomes larger than 10 deg. We used a position angle determined by peak pixels and an axis ratio determined by ellipse fitting.

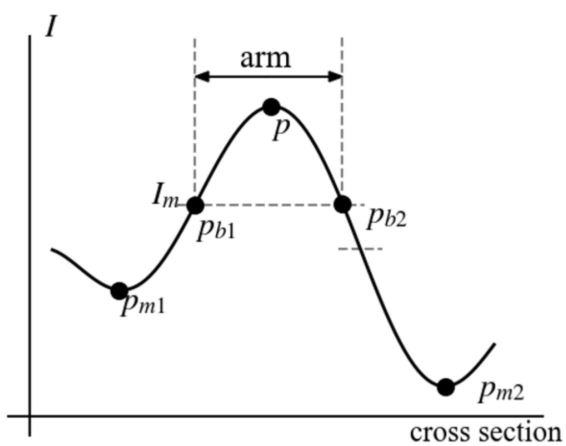

Figure 2: Arm width detection for one-dimensional image.

Next, widths of arms are determined. Figure 2 is an illustration of the method for one-dimensional image (for simplicity). The tangental direction of peak pixels is refered as arm direction. The perpendicular direction to the arm direction is refered as cross-sectional direction. Two edge points in cross-sectional direction are determined for each peak pixel, p. The nearest local minimum pixel from p in cross-sectional direction is determined as p_{m1}. The nearest local minimum pixel from p in opposite side of p_{m1} is determined as p_{m2}. Note that the three points are on the cross-sectional line in the order p_{m1}, p and p_{m2}, and the intensity from p to p_{m1} and that from p to p_{m2} decrease monotonically. The median intensity at p and p_{m1}, and p and p_{m2} is obtained as I_{a1} and I_{a2}, respectively. The stronger value of I_{a1} and I_{a2} is determined as lower limit of the arm I_m. The weakest pixel stronger than I_m between p and p_{m1} is a border pixel, p_{b1}. The corresponding pixel from p and p_{m2} is another border pixel, p_{b2}. If the difference of intensity is smaller than the noise in the image, not both p_{b1} and p_{b2} can be defined. In such case, a width of the arm at this peak pixel also cannot be defined. The reason we use the same threshold I_m for both side of the peak is due to the assumption that the same color is used as the both side border by visual inspection. If the borders of a pixel p cannot be determined, the width of the arm at p is determined as follows. Now, p is a part of peak pixel lines. A certain pixel located nearer to the center than p at the same peak pixel line as p, and determined the width successfully is refered as $p_{\rm in}$. That located more distant to the center than p is $p_{\rm out}$. 1) If there are both $p_{\rm in}$ and $p_{\rm out}$, in the pixels between $p_{\rm in}$ and $p_{\rm out}$, the width is connected smoothly the widths of two pixels. (figure 3a) 2) If there is only a pixel of $p_{\rm in}$ and $p_{\rm out}$, the width from the pixel to the edge of the arm is equal to that at the pixel. (figure 3b) 3) If there is neither $p_{\rm in}$ nor $p_{\rm out}$, this means that no pixel can be determined its widths. In this case, arm width determination is failed. In this method, arm width may be much different even in adjacent pixels. However, this property is not consistent with visual inspection. Therefore, arm width is finally averaged with adjacent two widths.

Figure 4 is a morphological feature map obtained from the local peak map shown in figure 1. The two arms and the bar are determined roughly corresponding to visual inspection. Since the width of each point of the arms is determined by avarage intensities of a local peak and local minimums, the width of the arms become larger toward the outer galaxy. Since NGC 3627 has strong arms, it is relatively easy to determine the widths of the arms. However, even for grand-design galaxy NGC 3627, these widths cannot be determined for many peak pixels. In addition, abrupt changes of widths are seen in the map. This method is fundamentally sensitive to pitch angle. Since the intensity change in the radial direction is much larger than in the angular direction, the width determination become very difficult when the cross-sectional direction of an arm

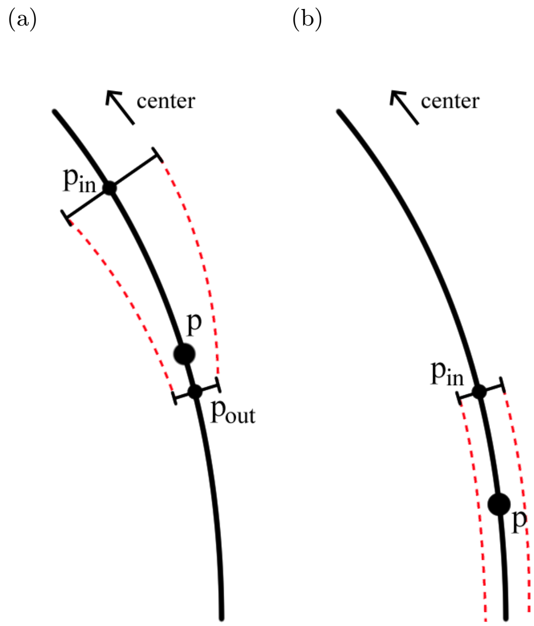

Figure 3: Illustrations to determine widths of an arm. Red dotted lines are interpolated or extrapolated arm boundaries. (a) The case that exists both p_{in} and p_{out}. (b) The case that exists only p_{in}.

is close to the radial direction.

2.2 Star formation and molecular gas analysis

The method shown in section 2.1 is applied to WISE 3.4 μm maps of the COMING galaxies. Morphological features are successfully identified in 12 galaxies. Whether the method is successfully applied or not is visually evaluated. In order to investigate star formation among morphological features, we additionally defined the galactic center region and bar-end regions. The galactic center region is located at the center of a galaxy and typically has a significantly higher intensity than other regions. The galactic center region is obtained by ellipse fitting similar to the bar definition, but it is determined as the largest ellipse whose ellipticity is larger than 0.95. The bar-end regions are both edges of the bar region picked up the 20 % tip along the major axis, and roots of arms connecting to the bar picked up the same length with the 20 % of the major

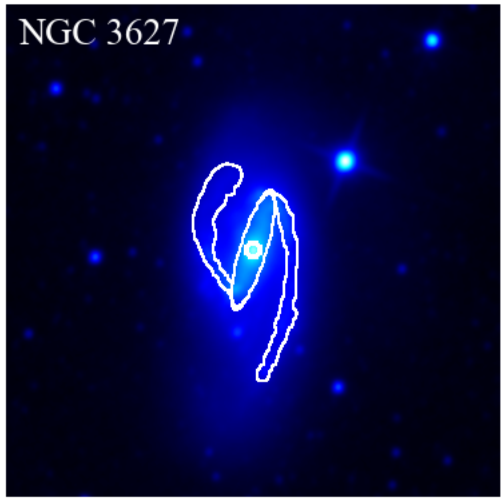

Figure 4: Structure border of NGC 3627 overlaid on WISE 3.4 μm maps.

axis length of the bar along the cross-sectional direction. Morphological feature maps of 12 galaxies are shown in figure 5.

Figure 4 is a SFE – velocity dispersion plot of each region of 12 galaxies. Velocity dispersions are obtained from COMING CO(1-0) moment-2 map by the full width of half maximum (FWHM) of velocity stacked channel map for each region. In velocity stacking, all velocity channels are shifted by the peak velocities, that is, shifted to 0 km s^{-1}. Each of the shifted velocity channel is summed up for each region, and these summed velocities are supposed to be a Gaussion function. The FWHM of the fitted function is defined as velocity dispersion. Note that the velocity dispersions obtained by velocity stacking for each region correlate with collision velocity of molecular clouds in the region, but the velocity dispersion on each region and the velocity of cloud-cloud collision are different. As the velocity dispersion increases, SFE increases in arm regions. However, SFE varies depend on galaxies in other regions which have larger velocity dispersion such as bar-end, bar and the central regions. Increases of velocity dispersion are generally thought to cause increases of the velocity and frequency of cloud-cloud collisions. However, it is reported that increases of the velocity dispersion do not necessarily result in SFE increases for NGC 3627 and NGC 4303 (Yajima et al. 2019). In their study, SFEs decrease with high veloc-

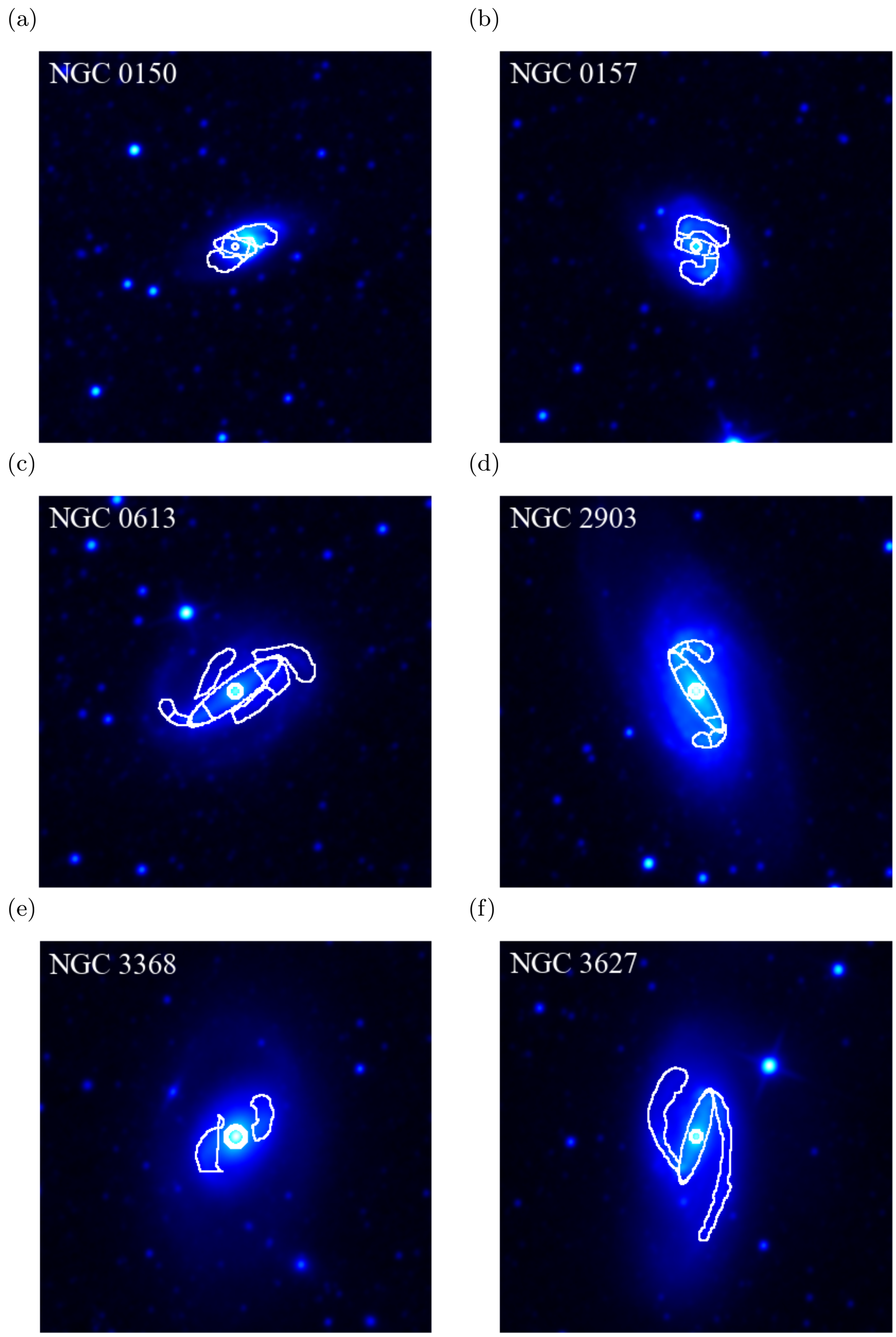

Figure 5: Structure border overlaid on WISE 3.4 μm maps of 12 galaxies.

(g)

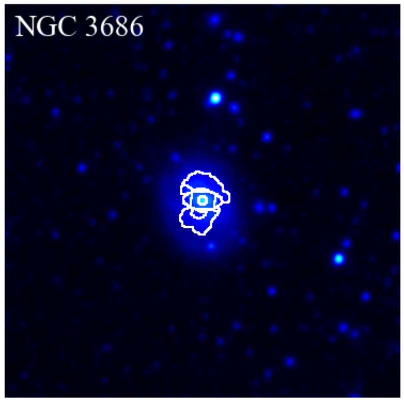

(h)

(i)

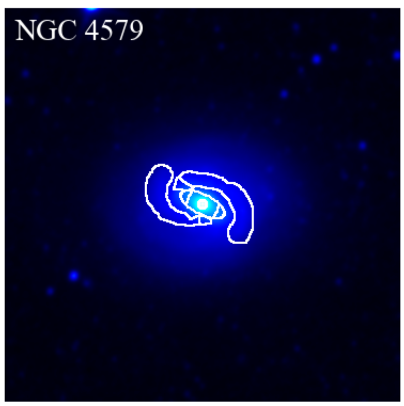

(j)

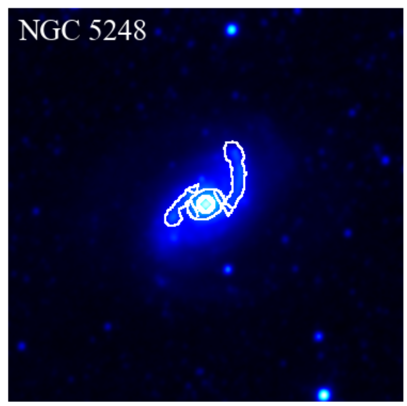

(k)

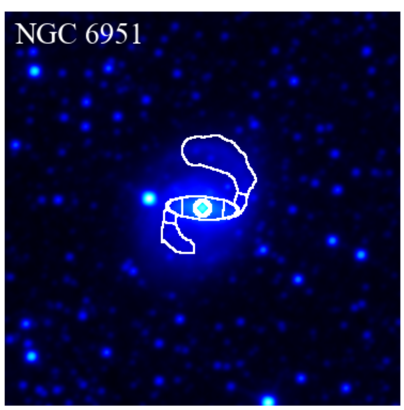

(l)

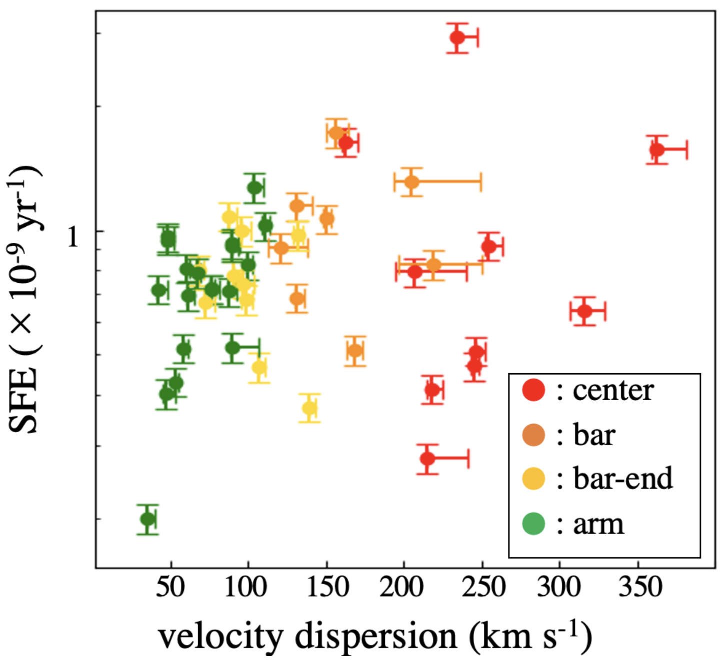

Figure 4: SFE–velocity dispersion of molecular gas plot for each regions of galaxies shown in figure 5.

ity dispersion since intense motion prevents the molecular clouds contracting, or causes intense collisions and destroys the clouds. In figure 4, some barred galaxies have a higher SFE in the bar region than that in the arm regions. However, the number of galaxies is too small to determine whether this SFE diversity is the general properties of bars or not. To solve the problem, it is necessary to successfully apply an image segmentation method to more galaxies. Therefore, we improve the method and aim to establish a method of morphological feature detection for more galaxies.

2.3 Application of image processing method

Feature determination by the method mentioned above is prevented by spatially large intensity change in the radial direction. In this subsection, we assume that high-frequency components in an intensity map constitute morphological features, and aim to extract only high-frequency components by the Fourier transform, the wavelet transform and the edge detection by an eigenvalue of Hesse matrix.

The Fourier transform is the method that transform information of positions into frequencies, and is expressed by the following equation.

$$\hat{f}(\xi) = \int_{-\infty}^{\infty} f(x)e^{-ix\xi}dx,$$

where $\hat{f}(\xi)$ is the Fourier transform of $f(x)$, x represents the spatial domain variable, ξ is the frequency domain variable, and $e^{-ix\xi}$ is the function that decomposes $f(x)$ into its frequency components. The Fourier transform is used for the determinaiton of the number of arms from the intensity of each mode to the polar coordinate plane. It is also used as a low-pass filter for noise reduction. We utilize the Fourier transform as a high-pass filter. That is, we mask pixels whose distances from the origin are smaller than the fixed value a in the Fourier space. After that, the inverse Fourier transform is performed. a is the frequency and corresponds to a reciprocal of the width of arms. In order to investigate the effectiveness of this filtering, low-frequency components of an intensity map of NGC 3627 is masked by various a. As a result, morphological features cannot be extract appropriately in any a. In addition, wave pattern appears throughout the image. The pattern is particularly pronounced for pixels with low intensity. It reflect the fact that they are represented as the sum of sine functions, which spread out infinitely in space.

Next, we investigate the effectiveness of the wavelet transform. The wavelet transform is the extension of the Fourier transform. The map is regarded as the sum of finite scale functions("wavelets"), not sine functions.

The wavelet transform is given by

$$W(a,b) = \frac{1}{\sqrt{a}} \int_{-\infty}^{+\infty} f(x)\psi^* \left(\frac{x-b}{a} \right) dx$$

where $W(a,b)$ is the wavelet coefficient of the function $f(x)$, $\psi(x)$ is the analyzing wavelet, $a(> 0)$ is the scale parameter and b in the position parameter. $\psi(x)$ is chosen depend on images. Morlet's wavelet, Mexican hat, Haar wavelet are widely used as wavelet functions. Each equation is given below.

$$\psi(x) = e^{-2\pi^2(\nu-\nu_0)^2} \quad \text{(Morlet}'\text{s wavelet)}$$

$$\psi(x) = (1-x^2)e^{-x^2/2} \quad \text{(Mexican hat)}$$

$$\psi(x) = \begin{cases} 1 & (0 \leq x < \frac{1}{2}) \\ -1 & (\frac{1}{2} \leq x < 1) \\ 0 & \text{(otherwise)} \end{cases} \quad \text{(Haar wavelet)}$$

where ν_0 is a constant. Note that the total energy (not intensity) in the image is preserved before and after the transform, which is known as Plancherel's theorem.

Starck et al. (1998) performed the wavelet transform to NGC 2997 intensity map, and emphasize morphological features. We applied the wavelet transform to many galaxies, and investigated the effectiveness of the wavelet transform. As a result, this method can hardly analyse many galaxies. The wavelet transform tends not to work well for galaxies with multiple spatial scales. For example, a map of a galaxy with a bold bar and thin arms can be hardly emphasized all features.

In order to solve the problem, the wavelet transform is applied repeatedly. Unlike the Fourier transform, the wavelet transform does not change the axes of an image before and after the application. Hence, the wavelet transform can be performed to the map after the transform. By the wavelet transform to discrete data (discrete wavelet transform; DWT), the map is divided into two, a map of smaller spatial scale than two pixels and that of larger spatial scale. The map is devided at each 2^n spatial scale. Here, n is the number of the transform application. Therefore, the wavelet transform can be used for images with multiple scales. However, there is a limitation for n due to the size of a map, since it is reduced by 1/2 each transform. The transforms are applied to WISE 3.4 μm maps. These maps are typically 438 $\times$ 438 pixels, and most arm widths are between 10 to 40 pixel.

As a result, we find that the wavelet transform does not work well for many galaxies. The separation by 2^n spatial scales are too rough to obtain the arm width difference. In addition, arm widths are too bold for the size of maps. For example, when a width of features is 16 pixel, the size of the map which divides the features is 27($\sim$ 438/16) pixels. It is too small to detect the features. The result is not improved by changing wavelet function and the map size by regriding or cliping. This result can be expected to improve for more high-resolution images. However, the feature detection method should be effective even for low-resolution maps since morphological features can be detected visually in WISE 3.4 μm maps. Therefore, we conclude the wavelet transform is not work enough for the morphological feature detection method.

The Hessian matrix is a square matrix created by the second-order partial derivative. The Hessian matrix for a pixel at (x, y) in a two-dimensional intensity map is represented by the following equation:

$$H(x,y) = \begin{bmatrix} \frac{\partial^2 I(x,y)}{\partial x^2} & \frac{\partial^2 I(x,y)}{\partial x \partial y} \\ \frac{\partial^2 I(x,y)}{\partial x \partial y} & \frac{\partial^2 I(x,y)}{\partial y^2} \end{bmatrix}$$

where $I(x, y)$ is the intensity at (x, y). Generally, for discrete two-dimensional data such as digital image, the derivative is obtained from the difference of the intensities of neighboring pixels in each direction. Spatial scale focused on is depending on how much distance is considered as a “neighboring”. Each pixel of the map has maximum of two eigenvalues. If the pixel has two eigenvalues and both eigenvalues are larger than 0, it is the local peak. This is used for the edge detection for pictuces. Some astronomical studies use the one of eigenvalues of each pixel directly, and made an eigenvalue map from an intensity map. The eigenvalue map seems to be the map which emphasizes local gradients. We performed this method to WISE 3.4 μm intensity map. We visually determined the effectiveness of the eigenvalue maps for morphological feature detection. As a result, we cannot detect morphological features well by the eigenvalue maps. It is because following two reasons. 1) Which features are emphasized is depending on galaxies. When the spatial scale focused on by the Hessian matrix and that of the morphological features are much different, the matrix emphasizes unintended features. For example, when the spatial scale of the Hessian matrix is smaller than that of the features, only the edge of features is typically emphasized. Fundamentally, multiple scales in an image cannot be treated with by the Hissian matrix. 2) Appropriate threshold values of the eigenvalue map depend on features. It means that morphological features in the eigenvalue map cannot be masked by a single threshold value. Thus, we conclude that an eigenvalue map of the Hessian matrix is useful for the support of morphological feature detection by visual inspection. However, it can be hardly used for automatic image segmentation of morphological features.

3 Method

Some terms are first defined before the description of our method. Morphological features, such as spiral arms, are characteristic intensity changes in a galaxy image. In this section, only spiral arms and bars are regarded as morphological features; inter-arm regions or point sources are not regarded as features. For each pixel in the map, the intensity has a local component and a global component. A local component forms morphological features, whereas a global component does not. Intensity gradients with a single peak are referred to as structures like a two-dimensional Gaussian function. Our method determines the pixels of morphological features in the structure emphasized by separating an intensity map into the two types of component. The method can be divided into the following three steps.

1. Each value in an intensity map is separated into a local component and a global component.

2. Structures are labeled if they consist of morphological features.

3. Structures located in the central region of the galaxy are labeled as a bar-like region. The bar-like region is a bar or spiral arms that cannot be spatially resolved (the bar and inner spiral arms cannot be distinguished in an intensity map).

In our method, the intensity of an image is regarded as a superposition of low- and high-spatial-frequency components. In visual inspection, only high-spatial-frequency components are morphological features. High-spatial-frequency components form spiral arms and a bar and low-spatial-frequency components extend throughout the galaxy and can be represented by Sérsic's law. The superposition of low- and high-spatial-frequency components makes it difficult to establish a morphological feature detection method. Therefore, we separate these two components from the original intensity map. In the high-spatial-frequency map, we mask non-feature pixels using a single threshold. We then label the structure at the center of the galaxy as a bar-like region.

3.1 Target images

The input for our method is a two-dimensional image containing only one galaxy (i.e., there are no other galaxies, even if they interact). Galaxies whose structures are difficult to resolve visually (e.g., edge-on galaxies, galaxies with small apparent sizes) are excluded as targets. The effect of spatial resolution is discussed in Section 5. We try to identify the internal structures of a single non-edge-on galaxy with a moderate or larger apparent size.

3.2 Extraction of local structures

In visual inspection, morphological features are detected based on the color change corresponding to an intensity change. A steep change in color is recognized as the border of a morphological feature. The intensity change on a small spatial scale is much more important than the intensity value. For example, the intensity gradient in the radial direction exists throughout a galaxy and is a dominant component of an image. However, such gradual global components do not contribute to the detection of morphological features using visual inspection. The presence of such global structures makes it difficult to separate feature pixels and non-feature pixels. Thus, the intensity of a galaxy I is regarded as a superposition of local components I_{local}, which are classified as structures by visual inspection, and global components I_{global}, which gradually change all over a galaxy.

$$I = I_{\mathrm{local}} + I_{\mathrm{global}}. \tag{1}$$

Figure 5 shows the intensity maps of a galaxy. To clearly show our concept, a one-dimensional image (e.g., a cross section along one direction) is given. The intensity of a galaxy is the superposition of I_{local} and I_{global}. I_{global} components are dominant in the original intensity map. However, since these intensities change gradually, their contribution to the detection of morphological features using visual inspection is small. Although the intensities of local components I_{local} are much smaller than those of global components, their contribution to the detection of morphological features using visual inspection is much larger than that of I_{global} components since their intensities in the map change steeply.

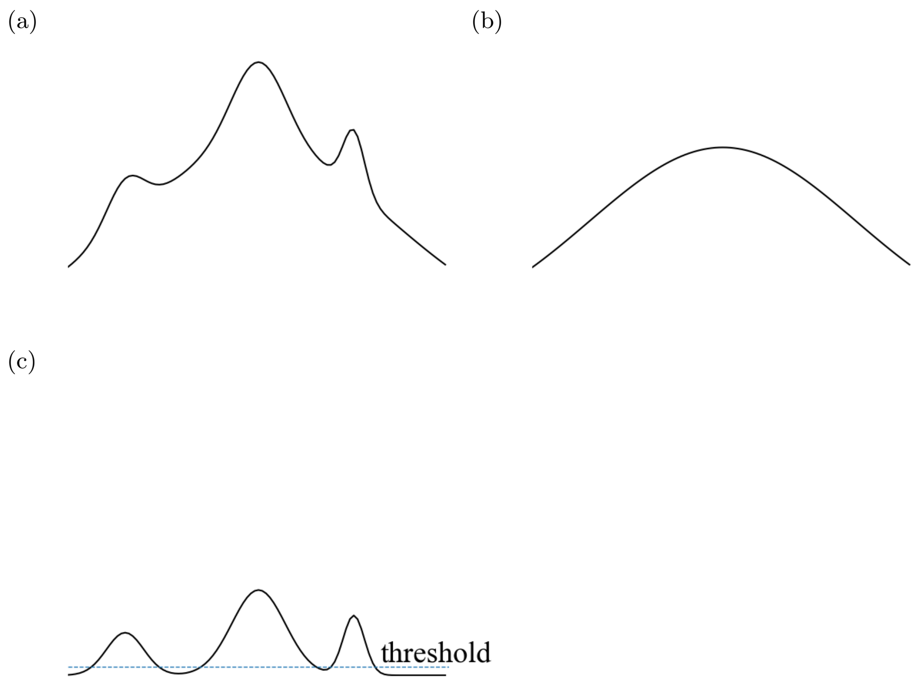

Figure 5: Intensity maps of galaxy along one direction. (a) Original intensity map. This map is the sum of global components (panel (b)) and local components (panel (c)). (b) Global components such as gradient in radial direction. (c) Local components such as spiral arms.

Since the feature components of galaxies are on a global component (shown as a curved line), a single threshold value (shown as a horizontal line) cannot separate structural components. If global components are subtracted from the original map, feature pixels and non-feature pixels become distinguishable.

Unlike Regan & Vogel (1994) that applied Sérsic's law to an image to obtain an $I_{\rm local}$ component map by subtracting $I_{\rm global}$ components, our method obtained an $I_{\rm local}$ component map independently of the shape of the local features; it is thus effective for more general galaxies. Here, spatial scale D is introduced to separate the global and local components. Structures spatially smaller than D are local structures and those larger than D are global structures. The method of determining D is described in detail in the next subsection.

First, we explain our method for one-dimensional images before we apply it to two-dimensional images. To obtain the intensities of global components for each position X on the one-dimensional line, $X = x$, each value of an intensity map $I(X)$ is expressed as a function of X (figure 6a). For each pixel P located at $X_{\rm P}$, neighboring pixels from P within D on the one-dimensional image are selected ($|X_{\rm P} - X| \leq D$). Pixels from $x - D/2$ to $x + D/2$ are selected (figure 6b). This small region is referred to as $\mathrm{R}_D(X)$. Next, boundary S is determined for each region $\mathrm{R}_D(X)$. Boundary S is the border of a local component and a global component; it is a line segment connected by two points for one-dimensional images (figure 6c). S is determined by two points, which are defined as follows: 1) minimum intensity point A in region $\mathrm{R}_D(X)$ (figure 6d); 2) point B, where the angle between line segment AB and the line $I = 0$ is minimum (figure 6e). The range in which S exists is determined as $\mathrm{R}_{\rm S}$. With the intensity of boundary S at X referred to as $I_{\rm S}(X)$, for all positions X inside region $\mathrm{R}_{\rm S}$, $I(X) > I_{\rm S}(X)$ must be satisfied since S is the border of two components for each pixel. In addition, since boundary S is around point P, $X_{\rm P}$ must be inside $\mathrm{R}_{\rm S}$. If the above is not satisfied, points farther from P in A and B are removed, the remaining point is renamed as A, and B is searched repeatedly until $\mathrm{R}_{\rm S}$ includes $X_{\rm P}$ or the length of $\mathrm{R}_{\rm S}$ is shorter than one pixel. In the latter case, boundary S at point P is undefined.

For two-dimensional images, $X = (x, y)$, the line plots for the one-dimensional case expand to surface plots (figure 7a, b) and a small region R that satisfies

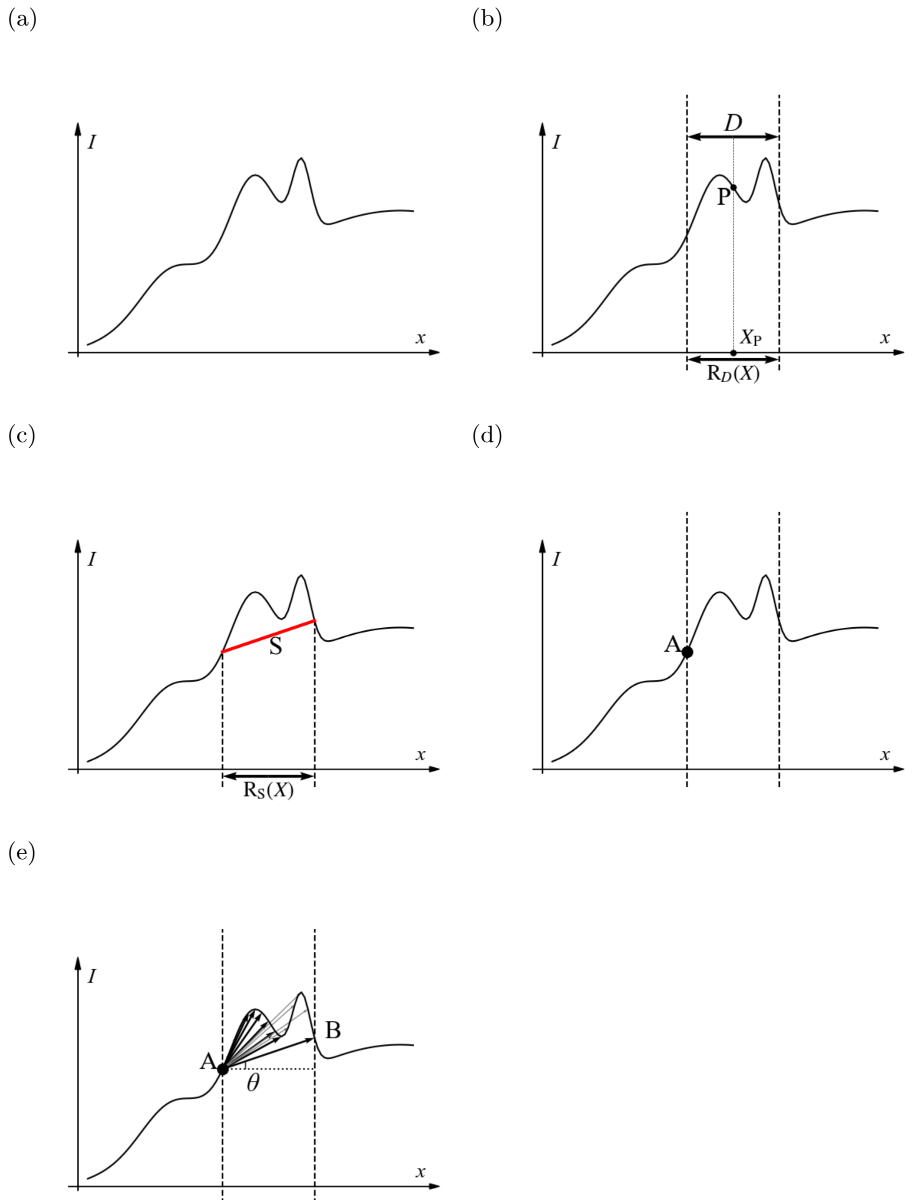

Figure 6: Boundary determination for one-dimensional image. (a) Line plot of one-dimensional image. (b) Range within D from P, denoted as region $\mathrm{R_D}(X)$. (c) Boundary S for separating global and local components around P. It is defined by points A and B. The range where S exists is denoted as region $\mathrm{R_S}(X)$. (d) Minimum point in R, denoted as point A. (e) Calculation of angles between x axis and each point. The minimum angular point is point B. At each location x inside region $\mathrm{R_D}(X)$, the intensities of line segments must be lower than those of the image.

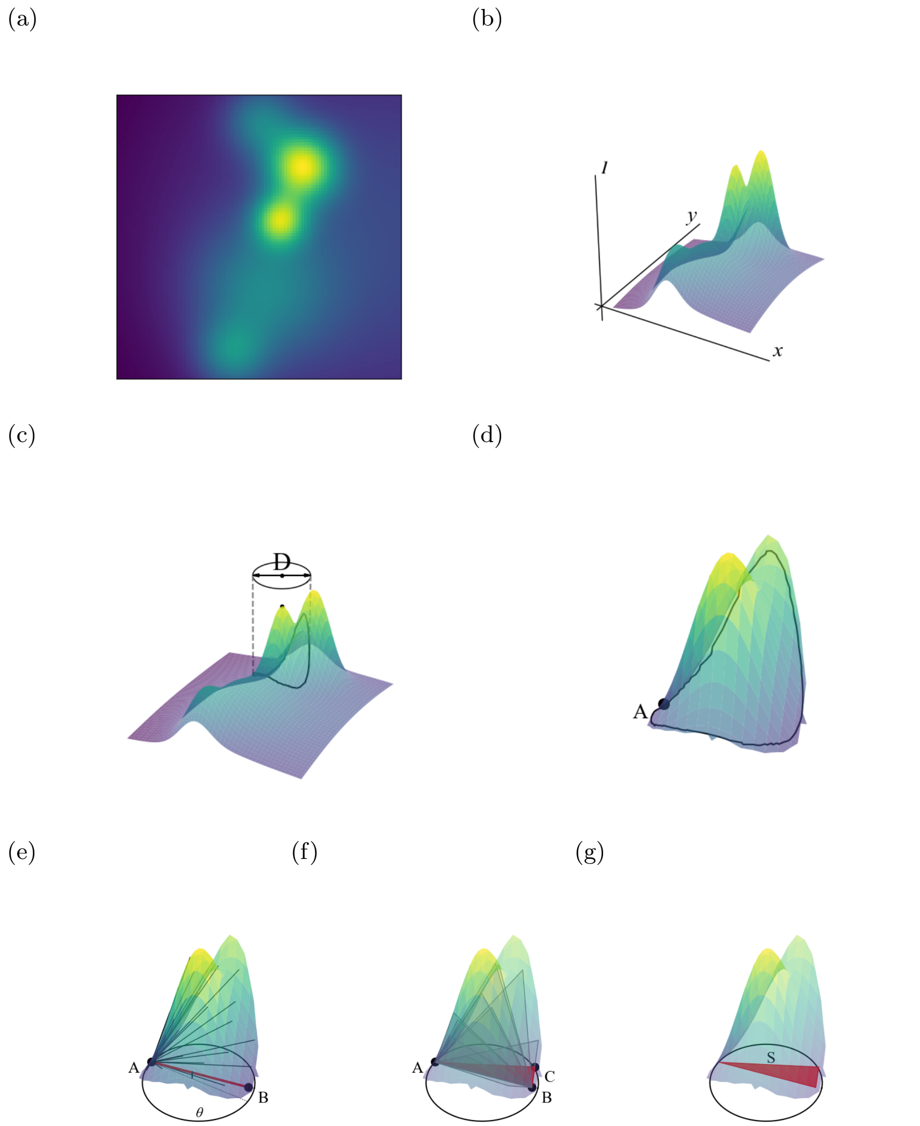

Figure 7: Boundary determination for two-dimensional image. (a) Original image. (b) Surface plot of two-dimensional image in x-y-I space. (c) Range within D from P, denoted as region R. (d) Extracted region R. The minimum point in R is point A. (e) Calculation of angles between x-y plane and lines through each point and point A. The minimum angular point is point B. (f) Calculation of triangles A and B and each point in region R. The angles between the x-y plane and each triangle are calculated. The minimum angular point is point C. All points of the triangles must be lower than the corresponding points of the image. (g) Triangle ABC is boundary S around P.

$|X_{\mathrm{P}} - X| \leq D$ is a circular region (figure 7c). Boundary S is determined as the plane that includes the following three points: 1) minimum intensity point A (figure 7d); 2) point B, where the angle between line segment AB and the x-y plane is minimum (figure 7e); 3) point C, where the angle between the x-y plane and the plane that includes ΔABC is minimum (figure 7f). As in the one-dimensional image case, for all positions X inside region $\mathrm{R_S}$, $I(X) > I_{\mathrm{S}}(X)$ must be satisfied and X_{P} must be included in $\mathrm{R_S}$. If the above is not satisfied, the farthest point from point P out of A, B, and C is excluded and the remaining two points are renamed as A and B, and point C is searched repeatedly until $\mathrm{R_S}$ includes X_{P} or the area of S is smaller than one pixel. In the latter case, plane S at point P is undefined.

Figure 8 shows boundaries S for various points P. The image is a surface plot of a certain part of an intensity map around a single structure on a global structure. Point $\mathrm{P_1}$, a border of circular region R, and triangle boundary S of $\mathrm{P_1}$ are shown in black. Point $\mathrm{P_2}$, a border of circular region R, and triangle boundary S of $\mathrm{P_2}$ are shown in red. $\mathrm{P_1}$ is located at the peak of the structure and $\mathrm{P_2}$ is located in the middle of the structure. The black points are the intensities of the boundaries and the x-y plane at the same location as $\mathrm{P_1}$. The red points are those at $\mathrm{P_2}$. The boundary of $\mathrm{P_1}$ can separate the local structure and the global structure since the region includes all pixels of the structure. The boundary of $\mathrm{P_2}$ cannot separate the local structure and the global structure well since not all pixels of the structure are included in the region. In other words, the intensities of incorrect boundaries are higher than that of the correct boundary since a weak part of the structure at the edge is not included. For points in the middle of structures, such as $\mathrm{P_2}$, the black boundary given by $\mathrm{P_1}$ can more correctly separate two structures. Therefore, if multiple boundaries exist at one point, we utilize the boundary whose intensity is weakest.

The process subsequent to that in figure 7 is shown in figure 9. In figure 9a, all S for each pixel P are shown in gray planes. The shapes of boundaries at pixels with no local structures are long and narrow. For clearer visualization, some S are shown in deeper color. Some X_{P} are included in more than one S. In this case, the minimum intensity value of multiple S at P is determined as the accurate border of a local component and a global component. Figure 9b

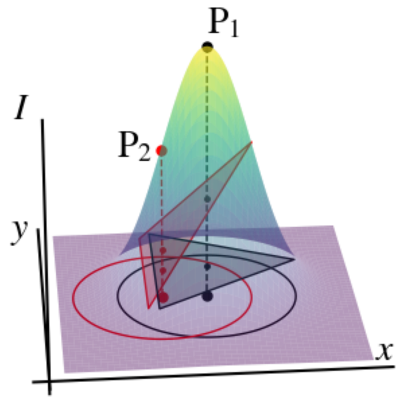

Figure 8: Boundaries S for each point P. The image is a surface plot of a certain part of an intensity map around a single structure. P_1 is located at the peak of the structure and P_2 is located in the middle of the structure. For the two points, the regions and boundaries (circles and triangles) are shown in black and red, respectively.

shows a surface of the minimum S in red. This surface is the border of local components and global components. Intensities below this surface correspond to the global component map. Figure 9c shows the local component map, which was obtained by subtracting the global component from the original intensity map.

3.3 Determination of spatial scale D

The sizes of morphological features in a galaxy are not constant. For example, the widths of spiral arms change within the galaxy. Thus, it is necessary to obtain the most appropriate spatial scale of structures D for each pixel. Figure 10 shows the principle of an accurate spatial scale determination process for a one-dimensional image (for simplicity). Figure 10a shows boundaries S for each D at position X. It is supposed that the appropriate size of the structure at position $D_a(X)$ is between the two fixed scales $D_{\min}$ and $D_{\max}$. That is, $D_{\min} < D_a(X) < D_{\max}$. These two scales, $D_{\min}$ and $D_{\max}$, are determined manually based on the conditions of the map, such as the map resolution and apparent galaxy size. When global components at all scales between $D_{\min}$ and $D_{\max}$ are obtained, the intensity of the global structure map changes its trend

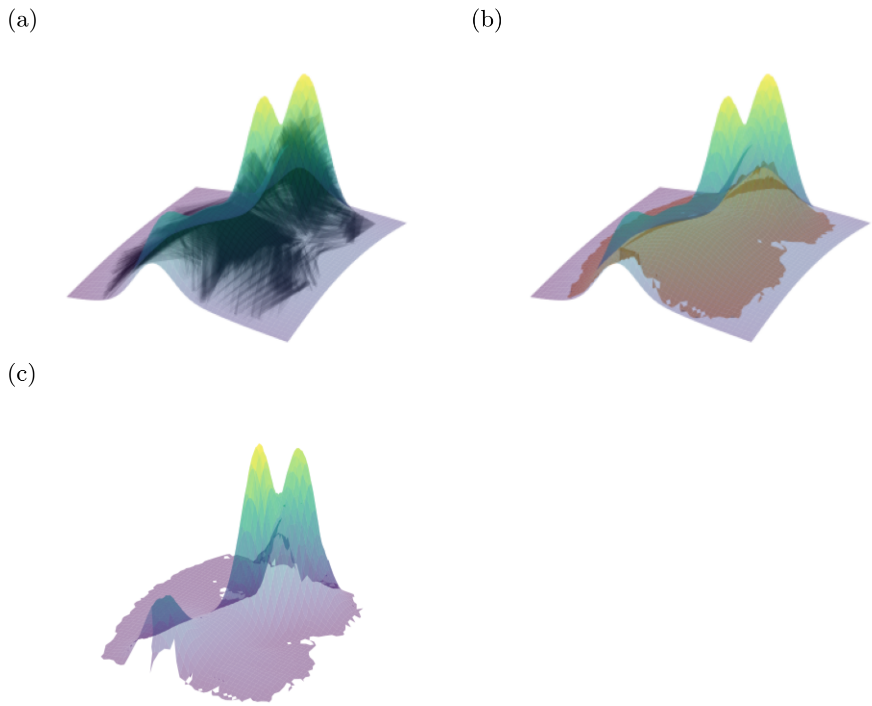

Figure 9: (a) Boundaries for each point in map in figure 7. Some triangles are shown in deeper color for clearer visualization. (b) Determination of boundary surface for separating global and local components. (c) Local component map. The global components in (b) were subtracted from the original intensity map in figure 7a.

around $D_a(X)$ for increasing D. When D is smaller than $D_a(X)$, the intensities of boundaries S become higher than the accurate boundary since not all pixels of the structure are included within boundaries S, as was the case in figure 8. When D is larger than $D_a(X)$, the same boundary as that of $D_a(X)$ should be determined. The change of S intensities with respect to D is shown in figure 10b. The y axis in figure 10b is the intensity of boundaries S in figure 10a. To accurately determine $D_a(X)$, the minimum S scale and the maximum S scale are connected by a line. These two scales do not need to correspond to $D_{\min}$ and $D_{\max}$ since S does not need to be determined at some D. At pixels for which fewer than three S can be determined, D_a cannot be determined. Next, the farthest point from the line is determined as $D_a(X)$ since the intensity trend changes at that point. $D_a(X)$ is obtained for all pixels in the image. The local components are extracted again with reference to $D_a(X)$ to obtain the appropriate D for all pixels. Lastly, the local component maps are convolved with a Gaussian kernel of diameter D.

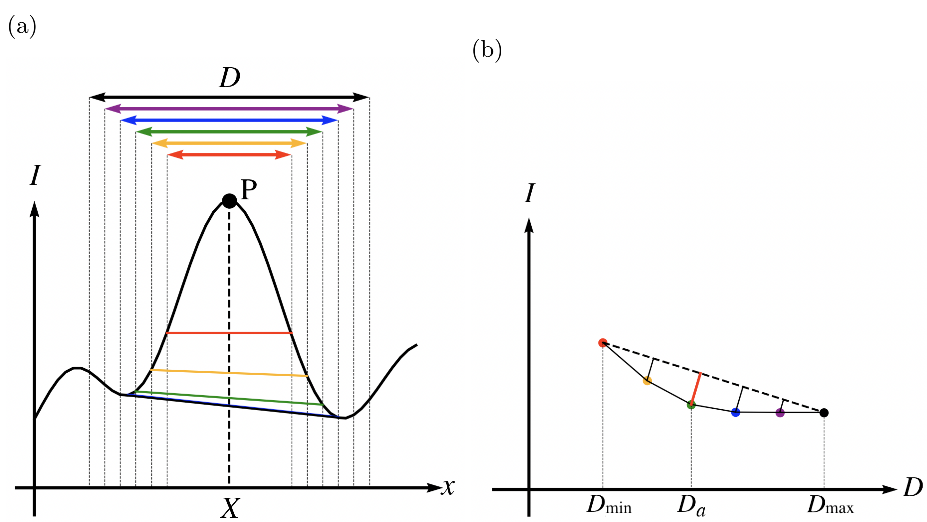

Figure 10: Concept for determining accurate spatial scale D around point P. (a) One-dimensional image and lines used to determine global components for each D value. (b) Global component intensity – spatial scale D plot. The farthest point from the line segment from the minimum D to the maximum D is determined as D_a.

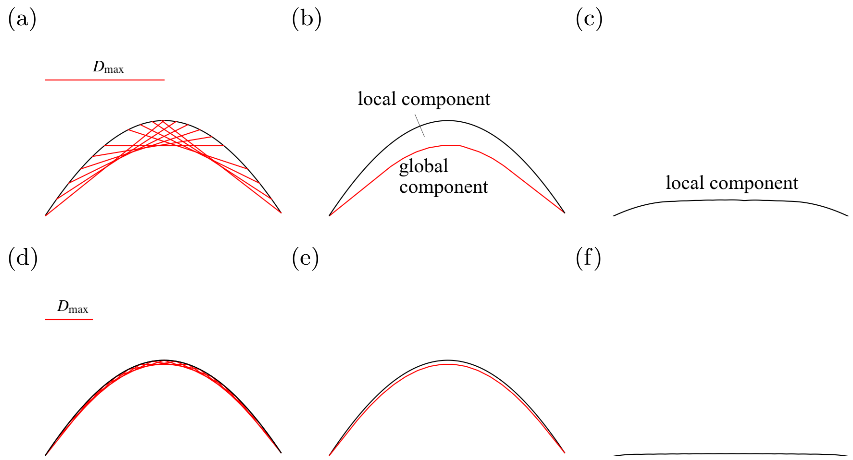

Figure 11: Subtraction difference according to $D_{\max}$ (top row). The scale of the structure is relatively small for $D_{\max}$. Red lines are boundary S for determining global components. (b) Global and local components. Since the lines do not completely trace the curve of the map, some local components remain. (c) Local component map. The bottom row is the same as the top row but the scale of the structure is relatively large for $D_{\max}$.

3.4 Definition of background pixels

Using the above process, we can obtain I_{global} map. I_{local} map can be obtained by subtracting I_{global} components from the original map. In the I_{local} map, morphological feature pixels and non-feature pixels can be distinguished by a single threshold. Since the subtraction of global components does not affect regions outside the galaxy, the standard deviation of the I_{local} map is effective as a threshold. However, there are two problems in applying this structure detection method to the local component map. First, the global component subtraction does not work well to a scale that is slightly larger than $D_{\max}$. Figure 11 shows the results of global component detection obtained using the method in figure 7 and 9 for a one-dimensional map (for simplicity). The upper row is the result of the application of the subtraction method to a relatively small spatial scale. This map has only one intensity structure and the scale of the image is larger than $D_{\max}$. Hence, in either line, all components should be detected as global components. However, a few parts of the global components are regarded as local components. Second, the trace of the intensity curve by line segments S has larger error at the structure when the structure has a slightly larger scale than D_{max}. For example, global components are not subtracted well in a local component map near the galactic center since the intensity change there is steep.

To overcome these problems, for each position in local map X, local intensity ratio $f(X)$ is defined and the intensity of the local map at each point $I(X)$ is multiplied by $f(X)$. $f(X)$ is defined as follows:

$$f(X) = \frac{I_{\mathrm{local}}(X) - I_{\mathrm{local,min}}(X, D_{\mathrm{max}})}{I_{\mathrm{local,max}}(X, D_{\mathrm{max}}) - I_{\mathrm{local,min}}(X, D_{\mathrm{max}})} \tag{2}$$

where $I_{\mathrm{local,min}}(X, D)$ and $I_{\mathrm{local,max}}(X, D)$ are the minimum and maximum intensity values, respectively, of region R, which is a small region of the map within range D from point X. Figure 12 shows the decrease of global components by $f(X)$. For each point P, $f(X)$ is calculated using local maximum intensity $I_{\mathrm{local,max}}(X, D_{\mathrm{max}})$ and local minimum intensity $I_{\mathrm{local,min}}(X, D_{\mathrm{max}})$ in a range that has a width of D_{max}. By multiplying the intensity of each point by $f(X)$, remnants of global components in the local component map are decreased and weak local components are emphasized. For example, the intensities of inter-arm regions near the galactic center are decreased and those of weak spiral arms in the outer region of a galaxy are increased. In addition, the emphasis by $f(X)$ does not affect most pixels not located near the galaxy or point sources. Therefore, after this process, the standard deviation is still effective for distinguishing morphological feature pixels and non-feature pixels. However, some strong point sources remain in the map. These structures are removed, as described later (see subsection 3.6).

3.5 Definition of central pixel of galaxy

To determine the bar-like region, the galactic center region needs to be determined since the center of a bar-like region is equal to the galactic center. The galactic center has a high intensity in both local and global components since many high-intensity structures with various scales are superposed at the galactic center. The galactic center pixel is determined as the pixel that satisfies the following two conditions: 1) the intensity of the pixel is larger than those of the

(a) (b)

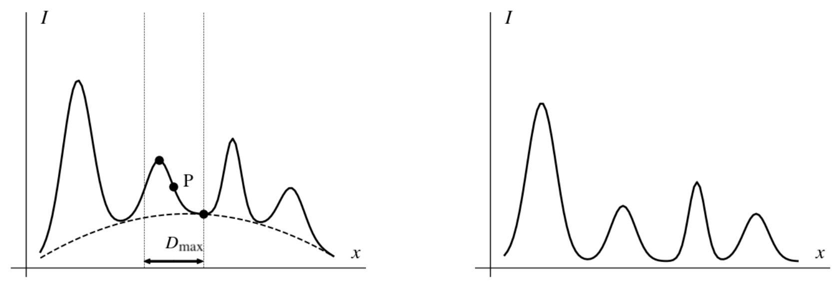

Figure 12: Decrease of remaining global component in local component map. (a) Local component map includes some parts of global component. For each point P, the intensity was normalized by the local maximum and local minimum inside a range that has a width of $D_{\max}$. (b) Normalized intensity map.

neighboring four pixels in the local component map; 2) the pixel is within $D_{\max}$ from the pixel where the sum of the intensities of pixels within $D_{\max}$ is the largest. Even if sources with higher intensities than that of the target galactic center (e.g., foreground stars in the Milky Way galaxy) exist in the image, the center of the galaxy can be selected if the spatial extent of the sources is smaller than that of the target galaxy. If point sources with a larger apparent size than that of the target galaxy exist in the image, our method cannot be applied.

3.6 Removal of non-feature pixels

A local component map is masked by the threshold determined in subsection 3.4. However, point source pixels are unmasked. Figure 13 shows the proposed non-feature pixel removal. Four criteria are used to remove non-feature pixels. As the first criterion, in the original map (figure 13a), pixels are masked if their intensity is lower than three times the standard deviation of the original map (figure 13b). This criterion is widely used for masking pixels outside galaxies. Pixels with a strong intensity are not removed by this criterion even if they are located outside galaxies. To remove such pixels, as the second criterion, regions isolated from other structures are removed (figure 13c). In the local component map, feature pixels are distributed as clusters surrounded by masked pixels. In this paper, we refer to a cluster of non-masked pixels connected to each other as

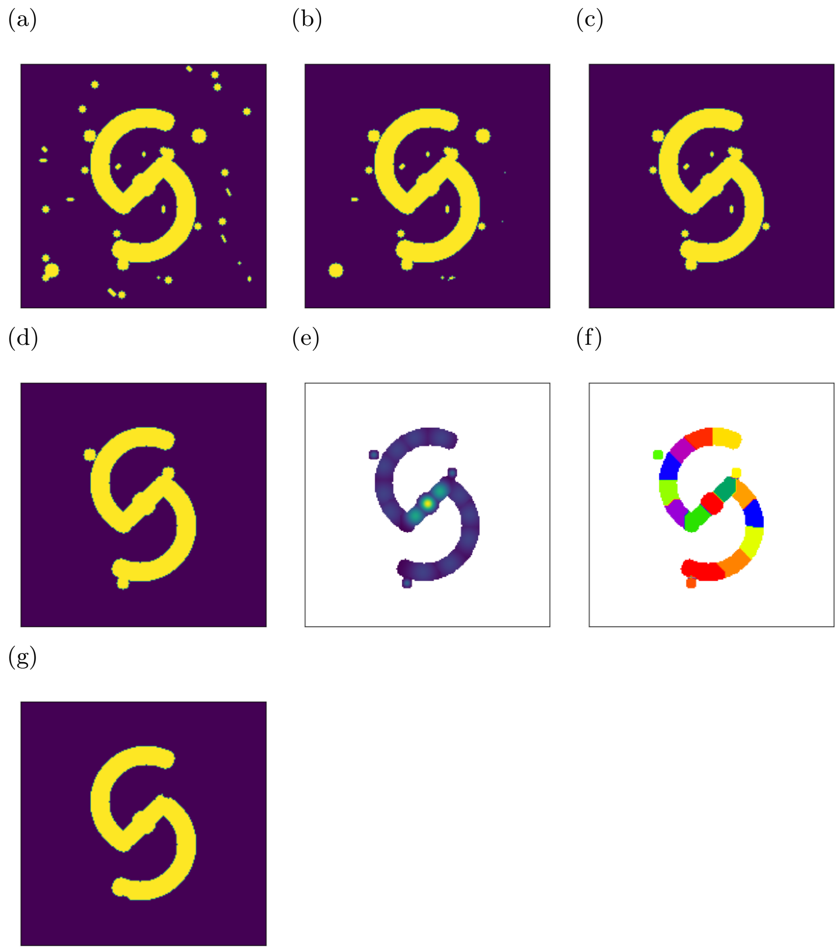

Figure 13: Steps of process used to remove non-feature pixels. (a) Map just after masking by standard deviation. Unmasked and masked pixels are shown in yellow and dark blue, respectively. (b) Mask obtained from original map masked by three times standard deviation. Using this, the map in (a) was masked. (c) Isolated structures masked. (d) Clusters with small widths masked. (e) Local intensity map. (f) Labeled map based on its intensity structure. Pixels in the same labeled structures are connected to each other. Pixels not connected to each other belong to different labeled structures even though they are shown in the same color. (g) Point source labels masked.

simply a cluster. Morphological features, especially spiral arms, extend from the galactic center or other arms. To decide whether a certain cluster is isolated, we use the friend-of-friend method. First, we find a morphological feature cluster that does not contain point source pixels. We regard a cluster that includes the galactic center as a morphological feature cluster. Clusters located near connected clusters are also morphological feature clusters. By repeating this process, clusters far from any other connected clusters are removed as isolated clusters. In this paper, the distance threshold for neighborhoods is set to $D_{\min}$ since gaps between clusters smaller than $D_{\min}$ are sufficiently smaller than the widths of spiral arms. The above process does not remove clusters inside the galaxy, such as small clusters located in inter-arm regions. As the third criterion, clusters are removed if the maximum widths are smaller than $D_{\min}$ (figure 13d). These clusters are not considered to be structures since $D_{\min}$ is the minimum scale of the structures. This criterion is for pixels belonging to non-feature clusters. When pixels are part of morphological feature clusters, they are not removed even if they are obviously non-feature pixels in visual inspection. Feature pixels and non-feature pixels are expected to belong to different structures. To remove non-feature pixels, the I_{local} map is labeled with each structure (figure 13e, f). This map is referred to as the labeled map. Since point sources are round in the intensity map, non-feature structures created by point sources in the labeled map are round and slightly connected to other labeled structures. Therefore, as the fourth criterion, in the labeled map, labeled structures are removed if their circumferences are approximately round and they are approximately surrounded by masked pixels. Whether the shapes of labeled structures are round-like is determined by ellipse fitting. If the ellipticity of labeled structures is more than 0.6 and more than 80% of the pixels inside the fitting ellipse are labeled pixels, then the labeled structures are regarded as round-like and removed. If more than 70% of the circumference pixels are connected to masked pixels, the labeled structures are also removed.

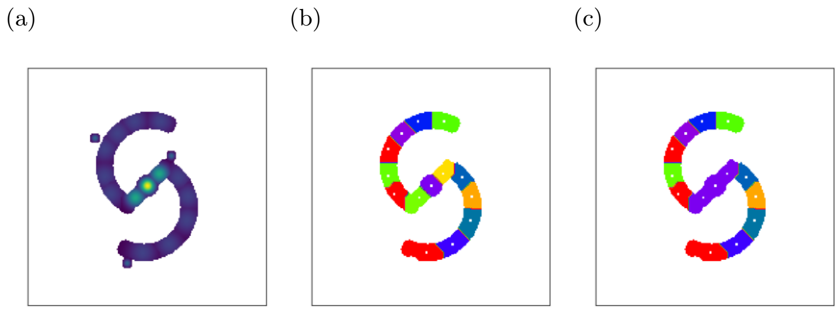

Figure 14: Process used to determine bar-like region. (a) Intensity map with masked point sources (same as figure 13). (b) Labeled map based on its intensity structure with peaks of each label (white points). If two labeled structures are connected to the central label and the peaks are at a location that is point-symmetric, these two labeled structures are joined to the central labeled structure. (c) Labeled map based on its intensity structure; same as panel (b) but bar-like region is united.

3.7 Bar-like region definition

After the removal of point sources, the local component map has only spiral arms and a bar-like region. The bar-like region is defined and separated from the spiral arms. Figure 14 shows the process used to determine the bar-like region. A labeled map, the same as that used for point source removal, is obtained based on the local intensity map to define the bar-like region. Since intensities around the galactic center in the local component map increase steeply toward the center, a single label is given to the area around the center. If the shape of a bar-like region is round-like, such as the bar of an SAB galaxy or the inward-extending arms of an SA galaxy, the central label is used for the bar-like region. However, if the shape of the bar-like region is elongated, such as the strong bar of an SB galaxy, the central label will not cover all pixels of the bar. The intensity distribution of the bar and the intensity peaks of the local map are both point-symmetric. Therefore, if two peaks of the labeled structures connected from the central labeled structure are at a location that is point-symmetric from the center, these labeled structures are defined as parts of the bar structure (figure 14b). This process is performed repeatedly to cover the entire bar.

4 Sample galaxies and data

To investigate molecular gas and star formation distribution among various morphological features, we targeted galaxies listed in the legacy project CO Multi-line Imaging of Nearby Galaxies (COMING), which was conducted with the 45-m telescope at the Nobeyama Radio Observatory (Sorai et al. 2019). COMING observed 147 galaxies, which is the largest number of galaxies used for a molecular gas mapping observation. The angular resolution of the survey data is 16.8 arcsec. The typical distance of COMING galaxies is 20 Mpc. The spatial resolution is 1.63×1.63 kpc at the distance. Parameters of the galaxies are shown in table 1 in the supplementary data section of the online version. We applied our method to WISE (Wright et al. 2010) band 1 (3.4 μm) images, which well reflect stellar distribution and are less affected by dust (Hackwell & Schweizer 1983). Note that our method is independent of image wavelength. The angular resolution of the WISE band 1 images is about 6.1 arcsec. The images are gridded at 1.375 arcsec. We set $D_{\rm min} = 11$ pixels and $D_{\rm max} = 41$ pixels based on the apparent size of the galaxies in the images. We set D to an odd number between $D_{\rm min}$ and $D_{\rm max}$ (i.e., $D = 11, 13, 15, ..., 41$) to target a centrosymmetric area in pixel units in the local component extraction.

5 Results

5.1 Global structure subtraction

Figure 15 shows the results of each process for SA galaxy NGC 628, SAB galaxy NGC 3627, and SB galaxy NGC 613. The global maps and maps for all sample galaxies are shown in the supplementary data section of the online version of this article. The first row in figure 15 shows WISE band 1 images (in logarithmic scale). The maps of global component $I_{\rm global}$ and local component $I_{\rm local}(= I - I_{\rm global})$ are shown (in logarithmic scale) in the second and third rows, respectively. The bottom row shows the logarithmic scale versions of the maps in the third row ($=\log_{10}(\log_{10} I_{\rm local})$) to emphasize the morphological structures in local maps. Each pixel in the local structure maps is convolved with a Gaussian kernel that has the same diameter as the structure scale of each pixel. The white pixels in the maps are pixels that any boundary S cannot be defined to determine the global component because these points are around a local minimum. These points do not affect structure detection because they are located outside structures.

For most galaxies that our method was applied to, morphological features were emphasized by subtracting the global components. For galaxies with very different intensities at the center and spiral arms, it is difficult to resolve inner structures by visual inspection. Our method resolves relatively inner regions. For some flocculent galaxies, our method can emphasize spiral arms that are difficult to identify by visual inspection.

Figure 16 shows the global structure maps for various values of D for NGC 3627. These maps were not convolved with their spatial scale. The white points in the maps are the points where no boundary S was determined. The number of white points decreases as D increases because pixels that cannot determine S have no local structures around them. All white points in the maps are located outside morphological features. The widths of morphological features of the galaxy, such as a bar, in the maps become larger correspond to D.

5.2 Accurate spatial scale determination

Figure 17 shows an accurate spatial scale D map of each pixel for NGC 3627. Hereafter, this map is referred to as a spatial scale map. Each pixel in this map has an accurate scale D_a (see figure 10). In the spatial scale map, D_a values change at the border of features since spatial scales at feature pixels and non-feature pixels are different. In addition, the values of spatial scales are small at the roots of the two spiral arms (region A1 and A2) and relatively large in the middle of the north-eastern arm (region B). This reflects the scales of the structures. There is no apparent pattern outside the galaxy. This reflects that there are no apparent local or global structures outside the galaxy. The values of the spatial scale are large around spiral arms (region C enclosed by two dashed ellipses). This means that no local structures smaller than $D_{\max}$ exist; there is only a large, monotonous intensity change in the radial direction. As a whole, the spatial scales of morphological features in the original map are reflected in the spatial scale map.

5.3 Morphological feature definition

Figure 18 shows the morphological feature maps of the three galaxies shown in figure 15. Red pixels are bar-like regions and blue pixels are spiral arms. The remaining pixels are white. For all three galaxies, the morphological features in the local maps and original maps are well extracted. NGC 628 is an SA galaxy with four intermittent spiral arms. Almost all features in the local map were extracted. A point source northeast of the center and strong point sources near the edge of the map were removed. Some point sources were not removed; they are classified as spiral arms. The bar-like region is defined as a round-like structure at the galactic center. NGC 3627 is an SAB grand-design galaxy with two asymmetrical spiral arms. These two arms were well extracted. In addition, the large point source northwest of the galaxy was extracted. However, the northern region of the bar was not classified as a bar but as a spiral arm. This was caused by a region where stars concentrated at the point. NGC 613 is an SB galaxy with a large, strong bar and multiple arms. The large point source north of the galaxy was not removed. However, since this point source is easily removed by visual inspection based on labeled map, this galaxy is evaluated as galaxies with all correct features in subsection 6.1. In the local map, all visible structures seem to be emphasized. In the structure map, part of the western arm was removed in figure 18 because this part is regarded as a point source connected to the arm region. The defined bar-like region approximately corresponds to the result obtained using visual inspection.

6 Discussion

In this section, we evaluate the morphological feature maps of the target galaxies using visual inspection to determine the tendency of galaxies that our method is suitable for. In addition, we obtain the relationship between SFR surface density and molecular gas surface density to investigate whether our method can be applied for analyses of differences in the physical properties of features.

6.1 Evaluation of feature maps

The determination of morphological features is affected by the widths of morphological features, widths of the gaps between features, relative intensity of features with respect to the surroundings, and intensity of point sources. Our method can treat multiple scales of morphological features as long as the scales are between $D_{\rm min}$ and $D_{\rm max}$. These two scales are determined by visual inspection. However, if the widths of the gaps between features are narrower than $D_{\rm min}$, features may not be separated since they may be regarded as a single structure (and thus not well subtracted). The widths of features and gaps are affected by spatial resolution and the relative arm strength of a galaxy. The relative arm strengths are obtained as intensities in local component maps. In addition, a strong and large point source in a map may be regarded as the galaxy center pixel even if it is not inside a galaxy as mentioned in subsection 3.5.

We examined the relationship between the results obtained using our method and these parameters. For the evaluation, only WISE 3.4 μm data for the sample galaxies of COMING shown in the sSupplementary data of the online version were used; other images or values of Hubble-type shown in previous studies were not used. We excluded the following types of galaxy: interacting galaxies, edge-on galaxies, galaxies without any visual features, and galaxies located near a large point source in the map. We evaluated morphological feature maps for 65 galaxies. The evaluation was performed by visual inspection. The obtained galaxies were classified into the following three classes: A) galaxies with the wrong arms, B) galaxies with the wrong bar-like region, and C) galaxies with all correct features. For galaxies classified as A, subtraction of the global components or masking of the local intensity map failed. For galaxies classified as B, the bar-like region did not cover the whole bar or covered a region larger than the real size. The numbers of galaxies classified as A, B, and C were 18, 30, and 17, respectively. Figure 19 shows some original maps and morphological feature maps of each evaluation. The maps for all sample galaxies are shown in the supplementary data section.

In this evaluation, the spatial resolution and arm strength are compared for each galaxy. The typical spatial resolution is a length of each pixel in kpc unit obtained by distance to target galaxies and angular resolution, and is corrected by disk inclination. These parameters were taken from Sorai et al. (2019). The arm strength is defined as the ratio of the median of intensities of arm or bar-like pixels to the standard deviation in the local map σ.

Figure 20 shows box plots of the spatial resolution and arm strength per evaluation. The left box represents galaxies without any visual features (hereafter referred to as no-feature galaxies); it is shown for comparison with the evaluated galaxies. The spatial resolution per pixel decreases in the order A to C. The median values of the classes are 0.24, 0.24, 0.23, and 0.17 kpc, respectively. The morphological feature determination was easier for galaxies with a finer spatial resolution. Therefore, our method can typically determine morphological features whose spatial resolution is finer than about 0.17 kpc. For arm strength, there is a clear trend in the median values, which are 1.35, 1.46, 1.67, and 1.59σ, respectively. Since the dispersions increase in the order A to C, the morphological feature determination was easier for galaxies with a stronger arm. From the median values of no-feature galaxies and A galaxies, our method can separate arm and inter-arm regions for galaxies whose arm strength is stronger than about 1.4σ.

6.2 Galactic center region and inter-arm region

To investigate the difference in physical properties among regions, a galaxy center region and an inter-arm region are defined. In the WISE 3.4 μm images, the central region is defined as the area within a radius of 6 pixels from the galaxy center pixel. This is determined from the angular resolution and grid size as the area within which the central star-forming region can affect. The border of the galaxy is defined as an ellipse. The pixels inside the ellipse that are not in the spiral arms, bar-like structure, or galactic center are defined as the inter-arm region. The border of the galaxy is defined by the parameters given in Sorai et al. (2019), but the radius is defined as the largest radius where the spiral arms exist. Since outer arms may not be detected in the feature map, this radius definition is needed to not regard outer arm pixels as inter-arm pixels.

6.3 SFR and molecular gas surface density

SFR is derived from far-ultraviolet (FUV) and band 4 (22 μm) intensities based on the following equation shown in Casasola et al. (2017) and Muraoka et al. (2019):

$$\left(\frac{\Sigma_{\rm SFR}}{M_{\rm sun}{\rm yr}^{-1}\ {\rm kpc}^{-2}}\right) = 1.59\cos i\left[3.2\times10^{-3}\left(\frac{I_{22\mu{\rm m}}}{\rm MJy\ sr^{-1}}\right)+8.1\times10^{-2}\left(\frac{I_{\rm FUV}}{\rm MJy\ sr^{-1}}\right)\right],$$

where $I_{22\mu{\rm m}}$ and $I_{\rm FUV}$ are the intensities of the WISE band 4 (22 μm) and FUV bands from the GALEX Ultraviolet Atlas of Nearby Galaxies (Gil de Paz et al. 2007).

For molecular gas, we use the ^{12}CO($J = 1 - 0$) data from COMING. The conversion factor $X_{\rm CO}$ is $2.0 \times 10^{20}{\rm cm}^{-2}({\rm K\ km\ s}^{-1})^{-1}$. The error of the gas is derived from the standard deviation of the background pixels defined by the parameters given in Sorai et al. (2019). If there is an insufficient number of background pixels in the observation area, the radius is decreased to the outermost feature pixel and then the standard deviation of the background pixels is obtained. The SFR and morphological feature maps are converted to a grid size of $6'' \times 6''$ of the COMING molecular gas data to compare the physical parameters for each region.

Figure 21 shows the SFR surface density–molecular gas surface density plot for each feature of galaxies (in logarithmic scale). The data are the galaxies with correctly determined features. The color of the data corresponds to the features. For the bar region, the marker of the data corresponds to Hubble-type galaxies. The SFE values are shown as black lines. In spite of the large dispersion, the data are roughly crowded in groups of morphological features regardless of galaxy. For each morphological structure in bar-like regions, SB galaxies tend to have a higher SFE than that of SAB galaxies; there is no difference in the arm region. That is, the higher SFE for SB galaxies in COMING reported by Muraoka et al. (2019) is restricted in the bar.

7 Conclusion

We proposed a pixel-by-pixel morphological feature determination method that emphasizes small spatial gradients based on objective criteria. This method needs only a single intensity map; no physical parameters and other maps are needed. In addition, the proposed method can treat multiple scales in a map. Multiple structures with different spatial scales can thus be determined. Morphological feature pixels and non-feature pixels are separated by a single threshold. Bar structures can be detected as a centrosymmetric intensity distribution. This can detect bars that are not an ellipse. 17 of 65 COMING galaxies were correctly determined using the proposed method. Parameter dependence for each evaluation of the feature map showed that our method typically works well for galaxies with a spatial resolution finer than about 0.17 kpc and an arm stronger than about 1.4 times of standard deviation of a local map. With this identification of morphological features in SFR surface density maps and molecular gas surface density maps adopted for the 17 correctly determined galaxies, the center, bar, spiral arms, and inter-arm regions have different trends and galaxies for a given feature have similar trends. The higher SFE value found for SB galaxies in COMING is caused by the higher star formation activity in the bar.

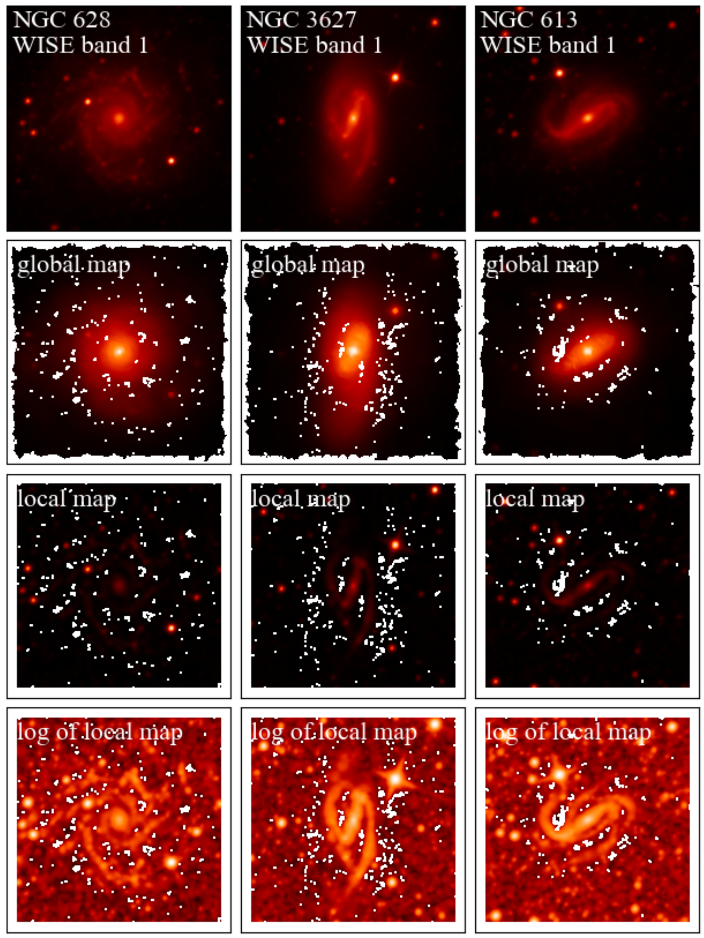

Figure 15: Subtraction of global component and extraction of local component for SA galaxy NGC 628, SAB galaxy NGC 3627, and SB galaxy NGC 613. The steps for each galaxy are shown in the corresponding column. First row shows the original WISE band 1 (3.4 μm) intensity maps (in logarithmic scale). Second row shows the global components of the images shown in the first row. No boundary is defined at white pixels. Third row shows the local components of the images shown in the first row. The global components were subtracted from the original map. Each pixel in the obtained local structure maps was convolved with a Gaussian kernel whose diameter was the same as the accurate spatial scale D_a. Fourth row shows the logarithmic scale version of the images shown in the third row to emphasize morphological structures.

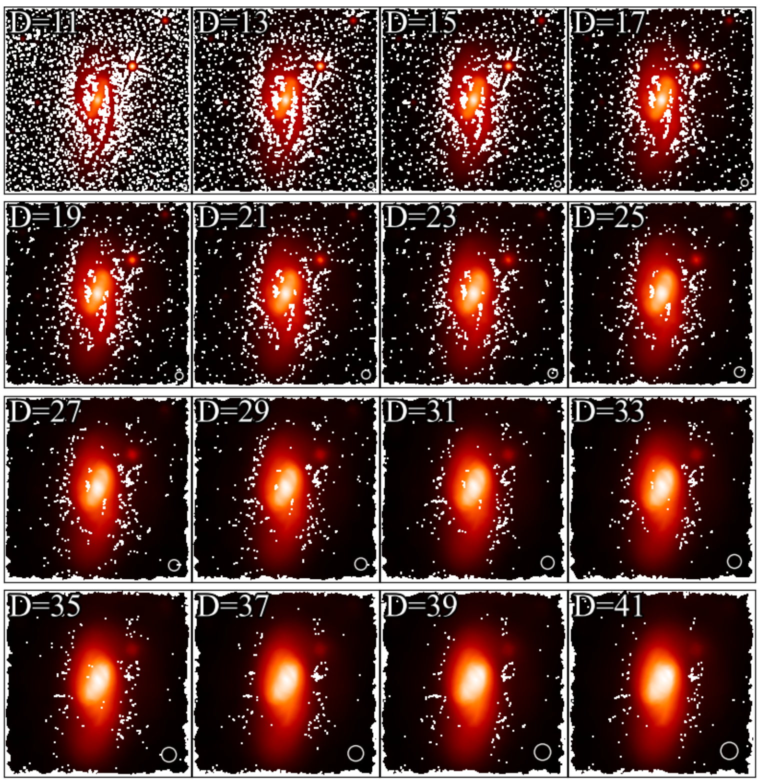

Figure 16: Global component map with fixed spatial scale D from $D_{\rm min} = 11$ to $D_{\rm max} = 41$. The maps are shown in logarithmic scale and not convoluted. White points indicate no data. Diameters of white circles at the bottom right are spatial scales D of each map.

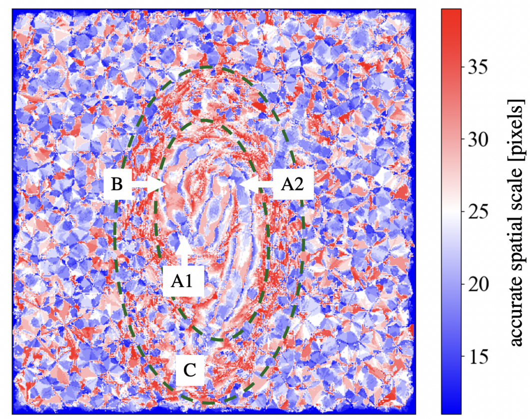

Figure 17: Map of accurate spatial scale D for NGC 3627.

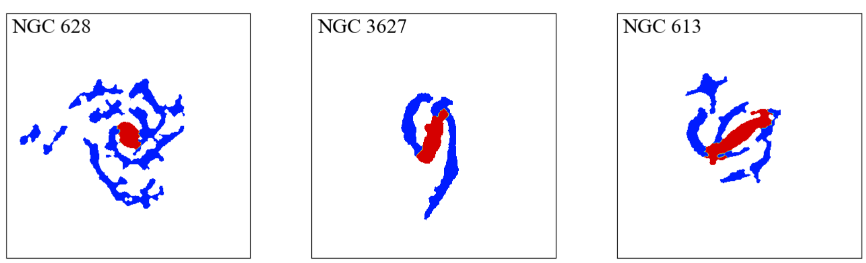

Figure 18: Map with labeled structures for NGC 628, NGC 3627, and NGC 613. Red regions: bar-like region; blue regions: spiral arms.

(a)

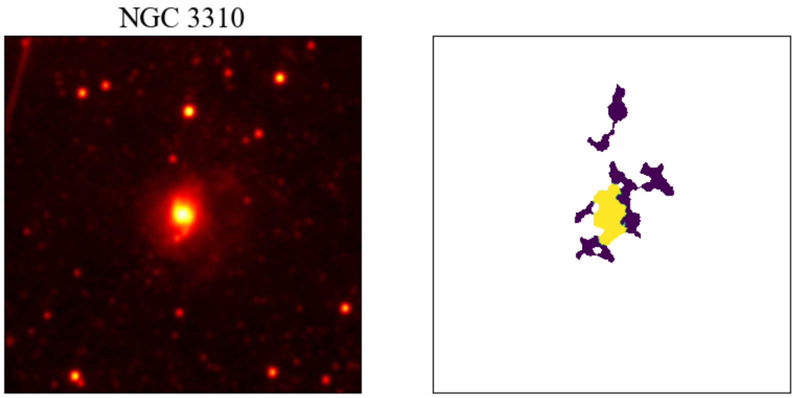

(b)

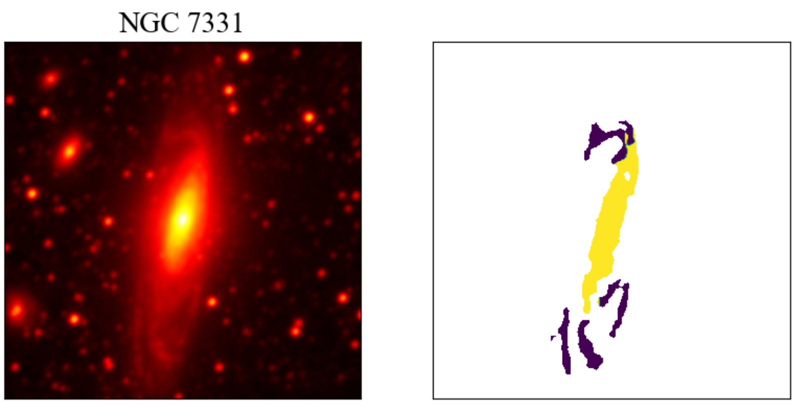

(c)

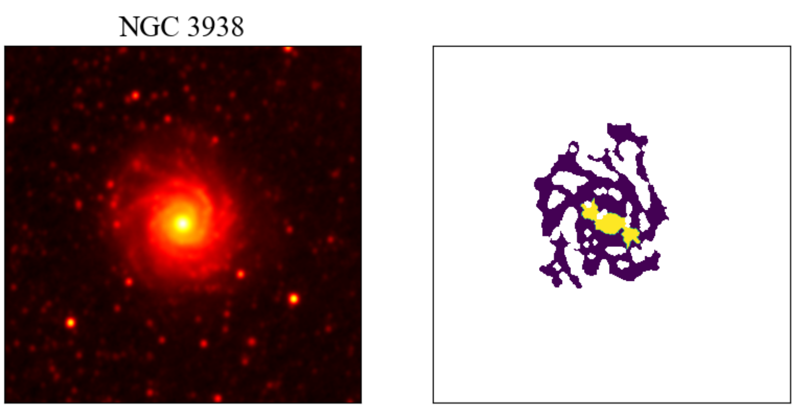

Figure 19: Some original maps and morphological feature maps. (a, b) Galaxies classified as A. (c, d) Galaxies classified as B. (e, f) Galaxies classified as C.

(d)

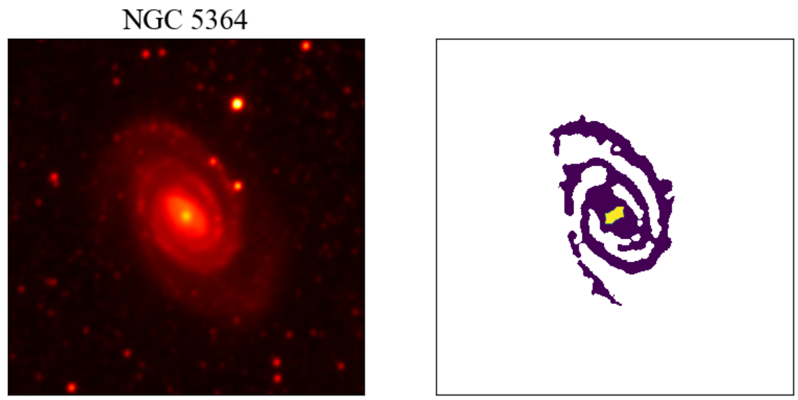

(e)

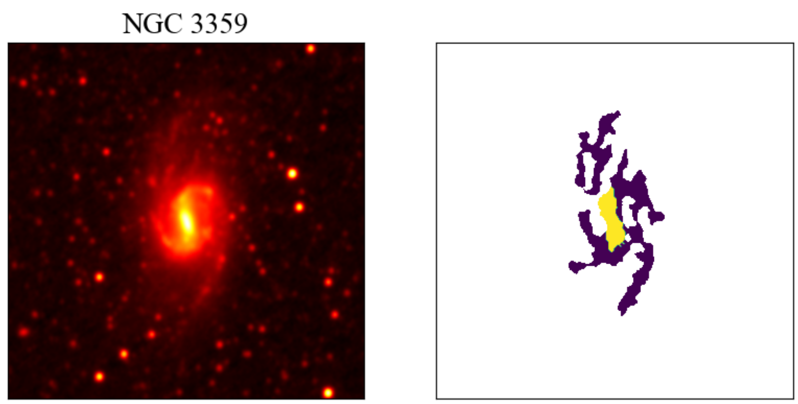

(f)

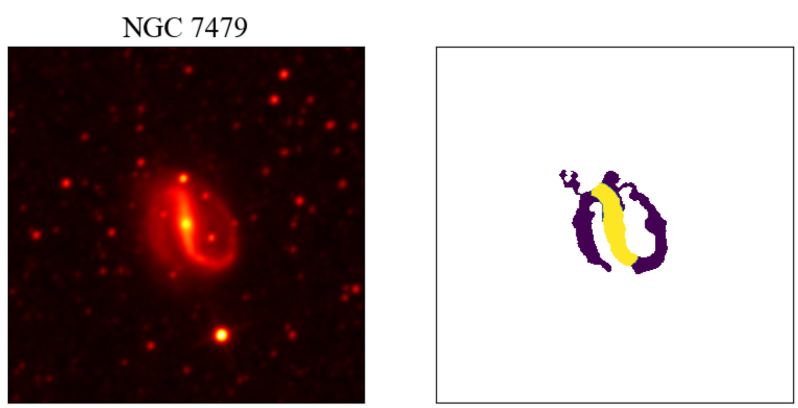

Figure 19: (Continued.)

(a) (b)

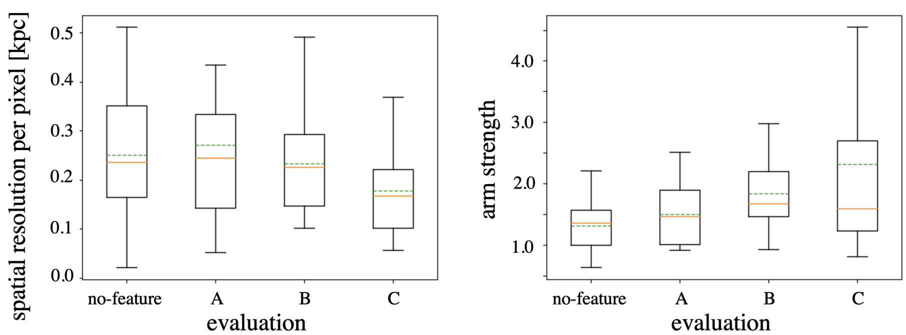

Figure 20: Box plots of (a) spatial resolution and (b) arm strength per evaluation. Solid lines are median values and dotted lines are mean values.

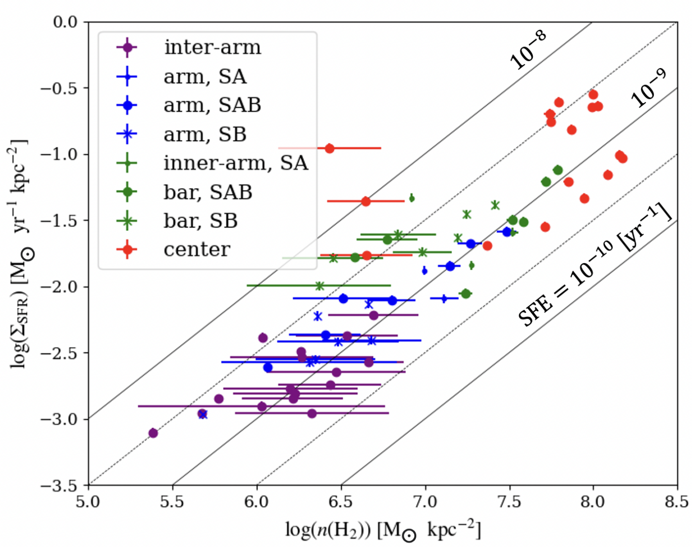

Figure 21: SFR surface density–molecular gas surface density plot for each feature of galaxies (in logarithmic scale).

References

Abraham, R. G., Valdes, F., Yee, H. K. C., van den Bergh, S., 1994, AJ, 432, 75

Abraham, R. G., et al. 1996, ApJ Suppl., 107, 1

Alfonzo, J. P., et al. 2024, ApJ, 967, 2

Baillard, A., et al. 2011, A& A, 532, A74

Bekki K. 2021, A& A, 647, A120

Bender, R., Doebereiner, S., & Moellenhoff, C. 1988, A& A, Suppl. Ser., 74, 385

Bershady, M. A., Jangren, A., Conselice, C. J., 2000, AJ, 119, 6

Casasola, V., et al. 2017, A& A, 605, A18

Conselice, C. J., Bershady, M. A., Jangren, A., 2000, ApJ, 529, 2

Conselice, C. J., 2003, ApJ Suppl. 147, 1

Danver, C. G. 1942, Lund Obs. Ann., 10, 1

Davis, D. R., Hayes, W. B., 2014, ApJ, 790, 2

de Vaucouleurs, G. 1959, Handbuch der Physik, 53, 275

Dressler, A. 1980, AJ, Suppl. Ser., 42, 565

Elmegreen, B., G., & Elmegreen, D., M. 1982, MNRAS, 201, 1021

Elmegreen, B., G., & Elmegreen, D., M. 1984, BAAS, 16, 454

Elmegreen, B., G., & Elmegreen, D., M. 1987, AJ, 314, 3

Fanaroff, B., L., & Riley, J., M. 1974, MNRAS, 167, 31

Egusa, F., Mentuch Cooper, E., ; Koda, J., & Baba, J. 2017, MNRAS, 465, 460

Gunn, J. E., & Gott, J. R. 1972, AJ, 176, 1

Hackwell, J. A., & Schweizer, F. 1983, ApJ, 265, 643

Hubble, E., 1926, ApJ, 64, 321

Iles, E. J., Pettitt, A. R., & Okamoto, T. 2022, MNRAS, 510, 3

Starck, J.-L. 1998, Image processing and data analysis

The multiscale approach, (Cambridge: Cambridge University Press), 1

Moustakas, J., Kennicutt, R. C. Jr., Tremonti, C. A. ; Dale, D. A., Smith, J.-D. T., & Calzetti, D. 2010, AJ Supplement Series, 190, 233

Kennicutt, R. C. 1983, AJ, 272, 54

Kennicutt, R. C. 1996, Starbursts: Triggers, Nature, and Evolution, (Les Houches: Les Houches School), 1

Kennicutt, R Leśniewska A., Michałowski, M. J., Gall, C., Hjorth, J., Nadolny, J., Ryzhov, O., & Solar, M. 2023, AJ, 953, 1

Lin, C. C., & Shu, F. H. 1964, AJ, 140, 646

Lotz, J. M., Primack, J., Madau, P. 2004, AJ, 128, 163

Mattia C. S., & Magorrian, J. 2015, MNRAS, 446, 4186

Momose, R., Okamura, S. K., Koda, J., Sawada, T., 2010, ApJ, 721, 1 Morgan, W. W., Mayall, N. O. 1957, Publ. Astron. Soc. Pacific, 69, 291

Muraoka, K., et al. 2019, PASJ, 71, SP1

Naim, A. et al. 1995, MNRAS, 274, 4 Ohta K., Hamabe, M., & Wakamatsu, K. 1990, AJ, 357, 71

Quejereta, M., et al. 2021, A& A 656, A133

Raddick, J., et al. 2007, BAAS, 39, 892

Regan M. W., & Vogel, S. N. 1994, AJ, 434, 536

Regan M. W., & Vogel, S. N. 1995, AJ Letters, 452, L21

Sánchez-Martín, P., García-Gómez, C., Masdemont, J. J., & Romero-Gómez, M. 2023, MNRAS, 520, 3909

Sandage, A. 1975, Publ. Astron. Soc. Pacific, 87, 853

Schade, D., et al. 1995, ApJ Letters, 451, L1

Slater, C. T., Bell, E. F., 2014, ApJ, 792, 2

Sorai, K., et al., 2019, PASJ, 71, SP1

Tanoglidis, D., Ćiprijanović, A., Drlica-Wagner, A. 2021, Astron. and Comput., 35, 100469

Tremonti, C. A., et al. 2004, AJ, 613, 898

van den Bergh, S. 1976, AJ, 206, 883

Vavilova, I. B., Khramtsov, V., Dobrycheva, D. V., Vasylenko, M. Y., Elyiv, A. A., & Melnyk, O. V. 2022, Space Sci. & Technol., 28, 1

Walmsley et al. 2022, MNRAS, 509, 3966

Wozniak, H., et al. 1995, A& A, Suppl. Ser., 111, 115

Wright, E. L., et al. 2010, AJ, 140, 1877

Yajima, Y., et al. 2020, PASJ, 71, SP1

Zavagno, A., et al. 2023, A& A, 669, A120

Arm segmentation

In this section, we consider how to divide the arm regions into respective arms. In other words, we aim to establish the method to detect a branch of arms. The method in this section is dismissed because of their inability to deal with the morphological diversity of galaxies, as described below. However, since the method is effective to galaxies with strong arms or simple shapes, we describe in detail here. The method is for the map after the feature segmentation shown in section 3 has been applied, that is, point sources have been removed and morphological features in the map are labeled as arm or bar-like. In the map, arm pixels are given a same label. In section 3, feature pixels are labeled as arm or bar-like based on their intensity. An intensity-based labeling is considered to be effective for arm segmentation since pixels with relative weak intensity are regarded as a boundary of morphological features by visual inspection. The boundary of each arm is the local minimum of intensity. Hence, the boundary of arms is also a boundary of labels in the labeled map. However, not all the boundary of labels are the boundary of arms. The labels belonging to the same feature is given a same label. In order to investigate the label belonging, following two methods are used: A) the method by skeleton map of an intensity-based labeled map; B) the method by dendrogram of an intensity map.

Skeletonization

Skeletonize function of Python sci-kit image library[1] is used in order to visualize the connections of each label. Skeletonization is a common image processing method for a binary image. It removes most outer pixels of objects in the image recursively to a single-pixel thickness, while preserves the topology and structure of the objects. The binary map after skeletonization is called to skeleton map. Skeletons are expected to trace the ridges of morphological features since these are found in the middle of arms. Hence, the intensities of the skeleton pixels are representative values for the arm intensities. Arm branching is obtained by connections of each label and the intensities of the skeleton pixels. However, some labels have no skeleton pixels, that is, some labels exist only around the

[1]https://scikit-image.org

boundary of a feature. These labels are not important for branching. Thus, they are united to another label in contact. If multiple labels are connected to the label with no skeleton, it connects to the label in contact that account for the largest portion of the circumference.

Then, the branching of labels with skeleton pixels are investigated. Labels connected with bar-like region defined in section 3 are the most inner labels. The connection of each label are traced to the outer edges of the arms. The following process are depending on the number of labels connected to a certain label (hereinafter called current label). 1) No label is connected to a current label. (figure 22a) In this case, the label is isolated and the process ends. 2) One label is connected to a current label. (figure 22b) The label is combined with the other label since the label is the edge of an arm. 3) Two labels are connected to a current label. (figure 22c) If the two labels are not in contact each other, tho two labels and the current label is arranged in a line. Hence, the current label and the inner connected label are combined. 4) Three or more labels are connected to a current label. In this case, the arm is branching. Since arms do not merge as one, there are a inner connected label and two or more outer connected labels. Now consider the case where there are two outer connected labels: L_1 and L_2. One of these is an extension of the current label's arm, while the other is another branched arm. For most galaxies, it is easy to determine the branched arm by visual inspection. This means that the intensities and the spatial distributions are different for each label. Then, which label is branching or not is determined in terms of intensity and position.

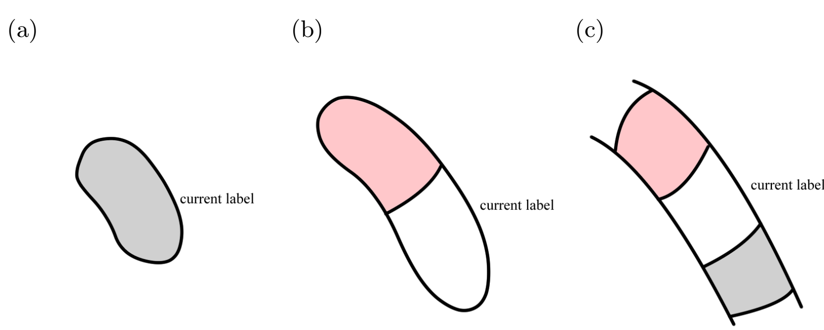

Figure 22: (a) No label is connected to a current label. (b) One label is connected to a current label. (c) Two labels are connected to a current label.

Firstly, the skeleton pixel with the highest value is obtained for each label, the current label and the label L_1 and L_2, and these points are refered as M_c, M_1 and M_2. Figure 23a is an illustration of this method. The minimum value on the skeleton pixels between the pixel M_c and M_1 is obtained. The minimum value between M_c and M_2 is also obtained. The label with the lower minimum value is able to be regarded as branching. This is because a strong gap of intensities tend to be regarded as a boundary of features. Even in the case that a current label has more connected labels, the label with the strongest minimum value is regarded as the outer extension of the arm which the current label is belonging to. Note that there is an intensity peak in a label, hence there is only one minimum value pixel between each intensity peaks.

Secondly, branches are determined by positions of each label. Consider the case where there are two outer connected labels L_1 and L_2, and these labels are extended from the current label. The current label has an inner connected label. The position of central pixel of the label is used for the position of the label. This can be obtained by regionprops function of Python sci-kit image library. The position angle from the inner label to the current label A_{i-c}, from the current label to the label L_1 and the label L_2, A_{c-1} and A_{c-2} are obtained. Figure 23b is an illustration of this method. The label with closer position angle to A_{i-c} is determined as the extension of the arm of the current label belonging to. This is because an arm does not change its direction abruptly. Since this method connects the centers of labels with straight lines, it does not work effectively for large labels.

Basically, a branch is determined by the method shown in figure 23a. Only if the lowest minimum intensity is larger than 90 % of the highest minimum intensity, the branch is determined by the method shown in figure 23b. This method works well for the galaxies with strong arms or simple shapes, while it does not work well for the galaxies with weak arms or rings. Here, rings include not only the full ring appeared in galaxies, but smaller ring-like structures.

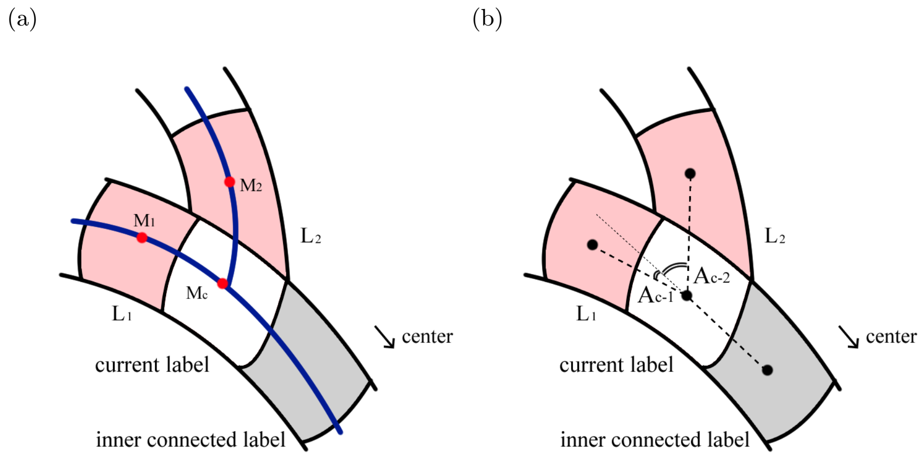

Figure 23: (a) An illustration of the method using intensities of skeleton pixels. (b) An illustration of the method using position angles of each label.

Dendrogram

To solve the problem, connections of each label is visualized by dendrogram. The dendrogram is made by Python ASTRODENDRO library[2]. This library creates tree structures from an intensity map and visualize an intensity distribution. Each peak in the map is defined as a leaf node. Branch nodes are the intensity where contour lines stem from different peaks unite. This library is typically used to detect high-density regions such as molecular cloud cores. It is now applied to morphological feature segmentation. This library can visualize peak label connection more properly than the method by skeletonize function, since more proper local minimum intensities are obtained.

As a result, an arm tends to be united to one branch. The result for NGC 628 is shown in Figure 24. However, there is no criterion to determine whether a branch is united arm or not, and the method also does not work well for galaxies with ring structures. In addition, this method is independent of other methods, difficult to combine other methods.

[2]https://dendrograms.readthedocs.io/en/stable/

(a)

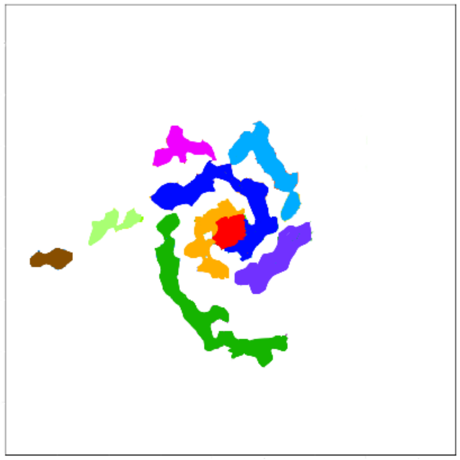

(b)

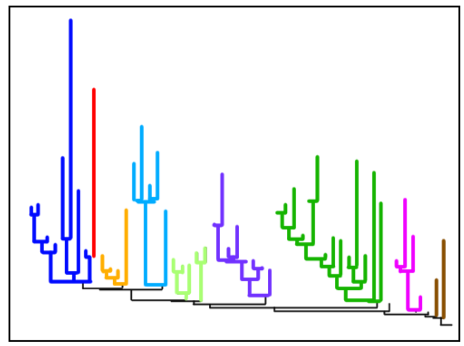

Figure 24: (a) A labeled map of NGC 628. Colors are corresponding to those in the dendrogram. (b) A dendrogram of (a).

Appendix: Maps of COMING galaxies

Figure 25 shows the maps of the COMING galaxies which can be seen the features visually. The left column is WISE 3.4 μm maps. The middle column is morphological features maps obtained from the map in left column. The right column is the same as the middle column but regrided to match the COMING data grid and added the central region and inter-arm regions. The evaluation of segmentation in the right column is at the top of the right figures.

(1)

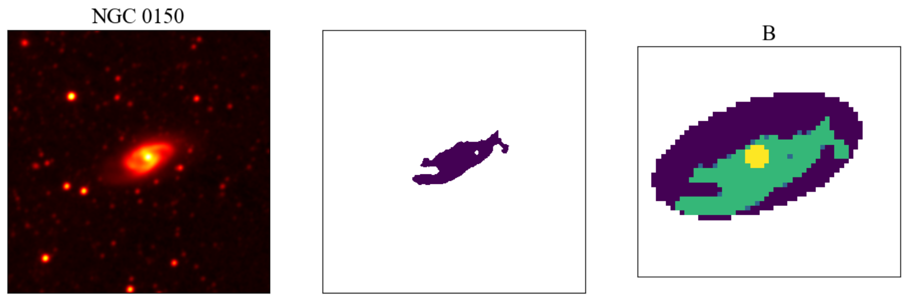

(2)

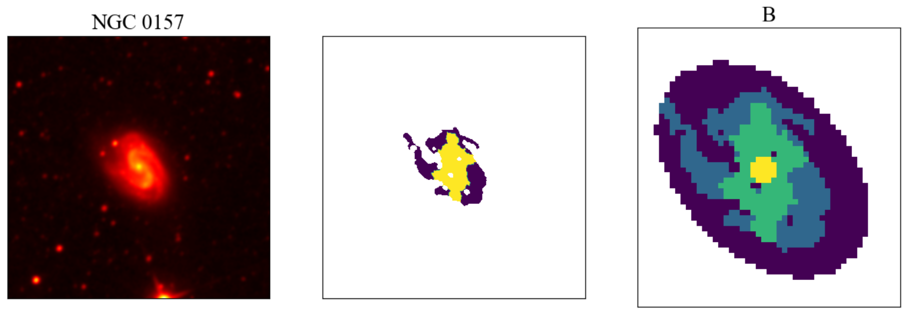

(3)

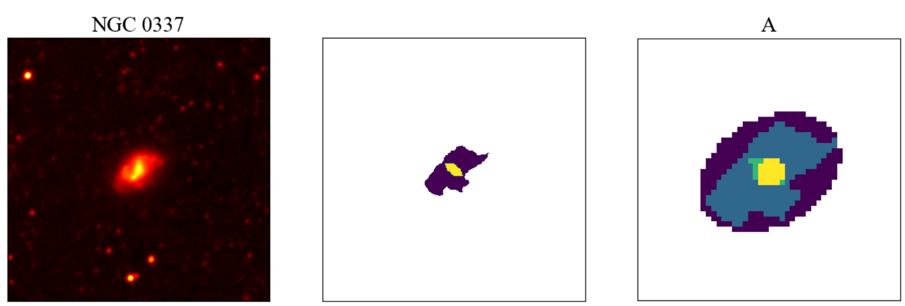

Figure 25: Maps of target galaxies. (left)WISE 3.4 μm map. (middle) Morphological feature map obtained from the left figure. (right) The same map as the middle but regrided to match the COMING data grid and added the central region and inter-arm regions.

(4)

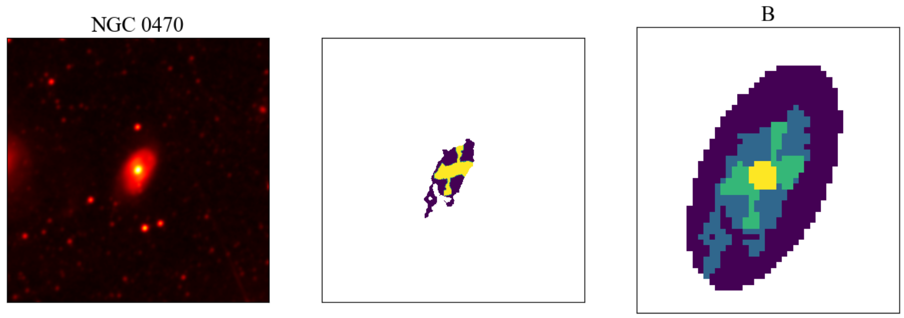

(5)

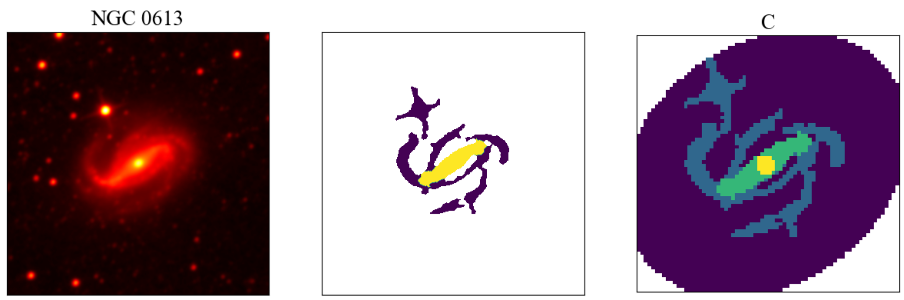

(6)

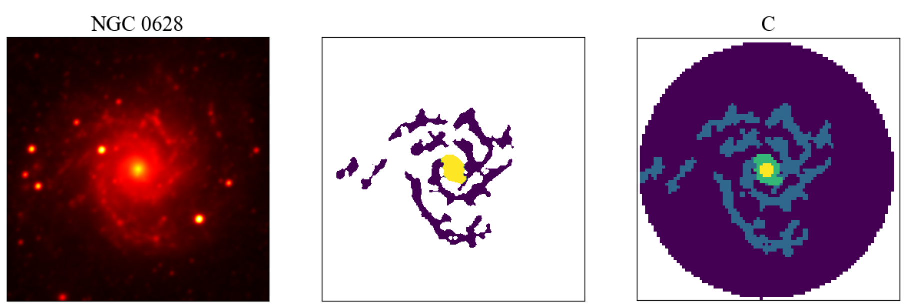

Figure 25: (Continued.)

(7)

(8)

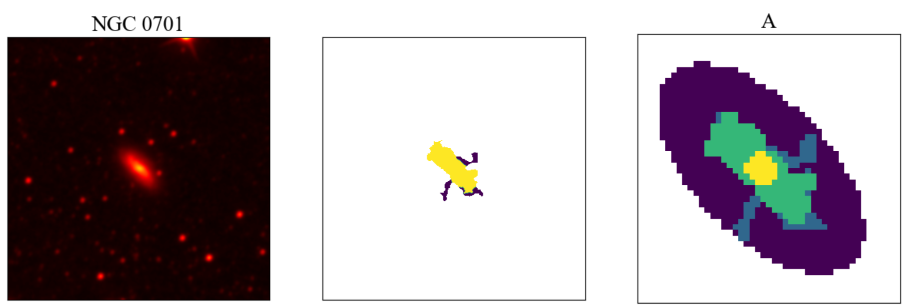

(9)

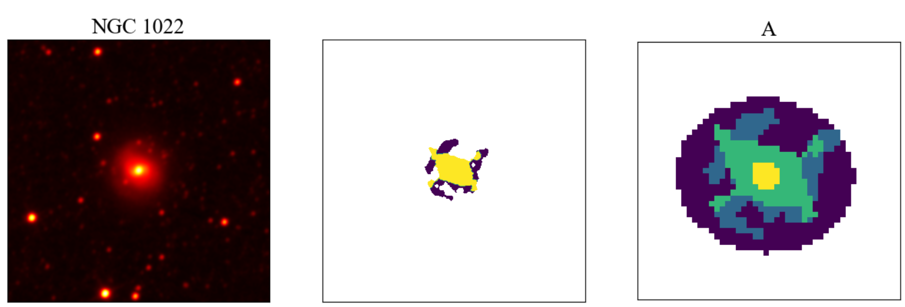

Figure 25: (Continued.)

(10)

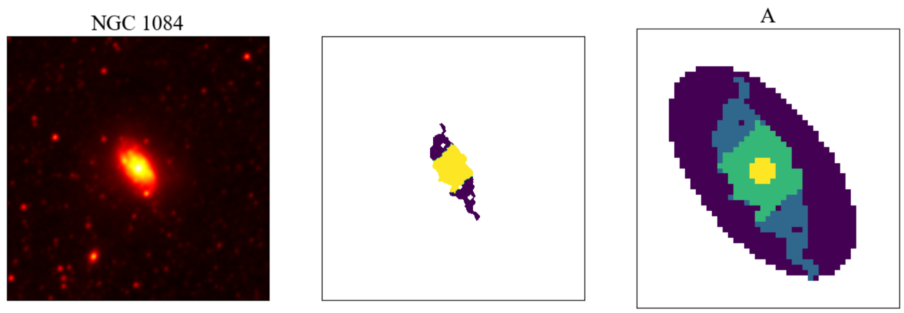

(11)

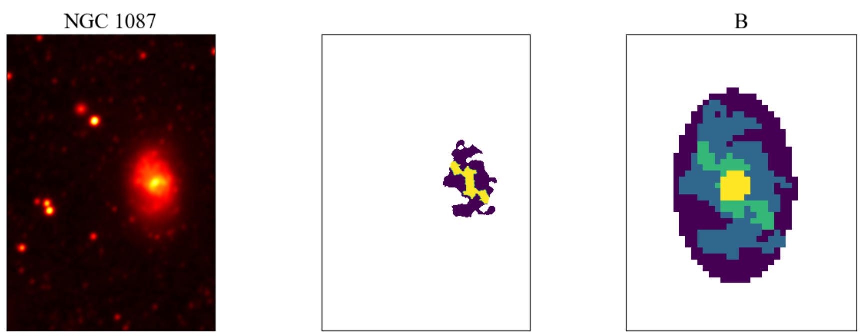

(12)

Figure 25: (Continued.)

(13)

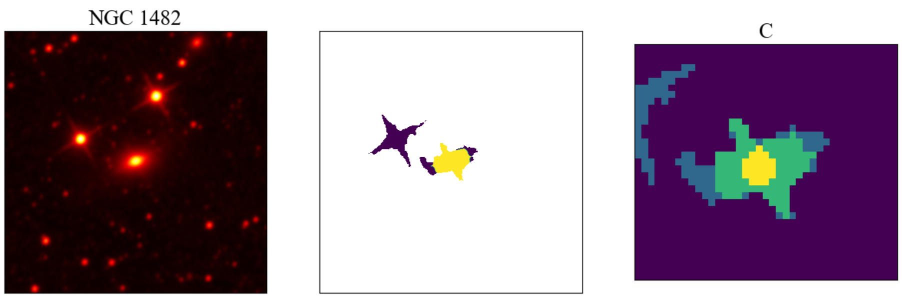

(14)

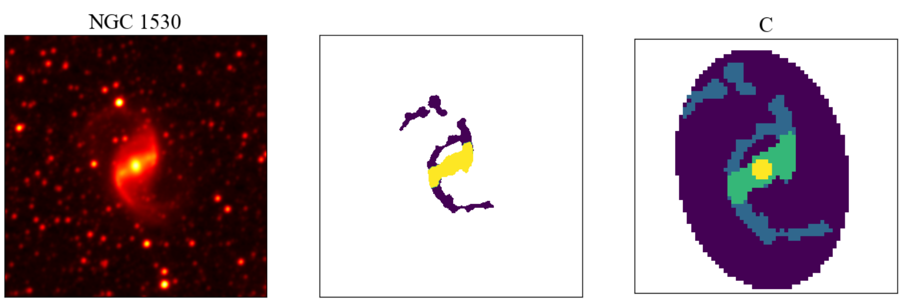

(15)

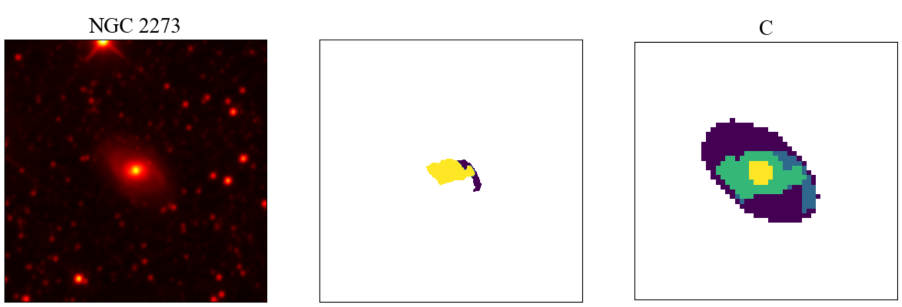

Figure 25: (Continued.)

(16)

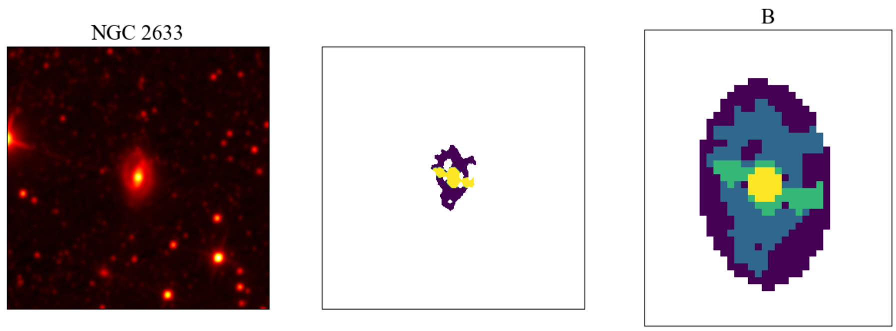

(17)

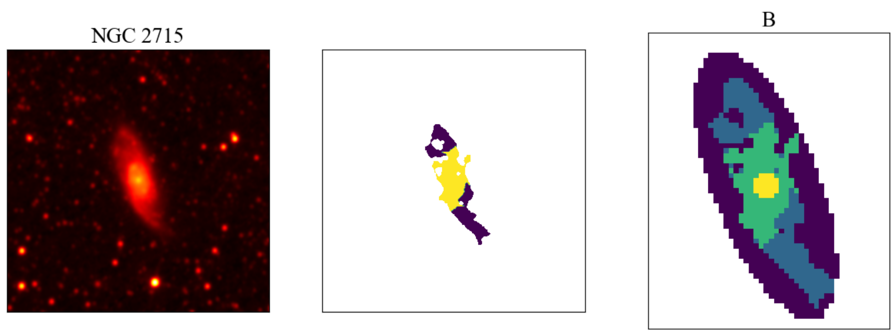

(18)

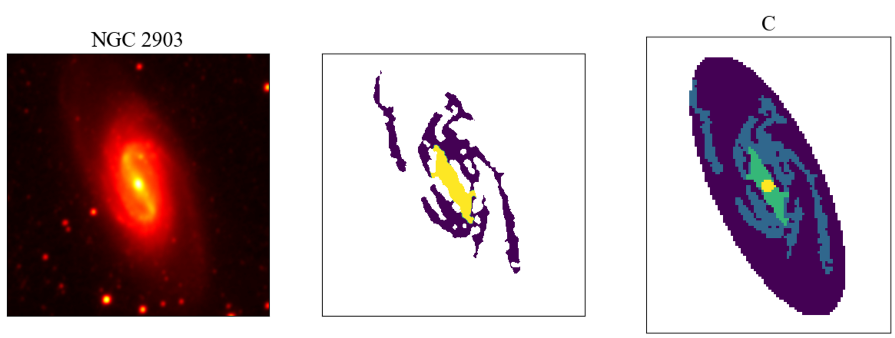

Figure 25: (Continued.)

(19)

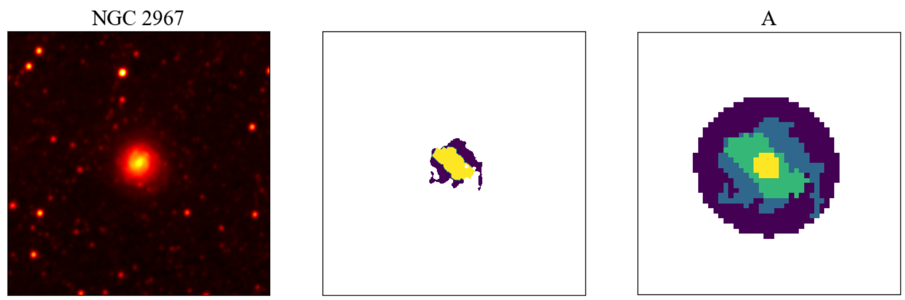

(20)

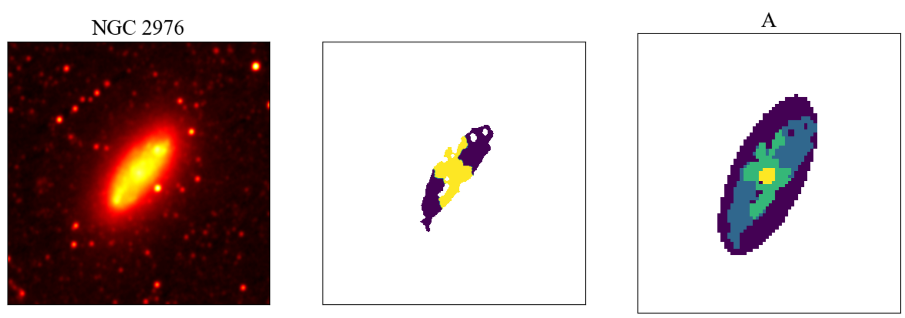

(21)

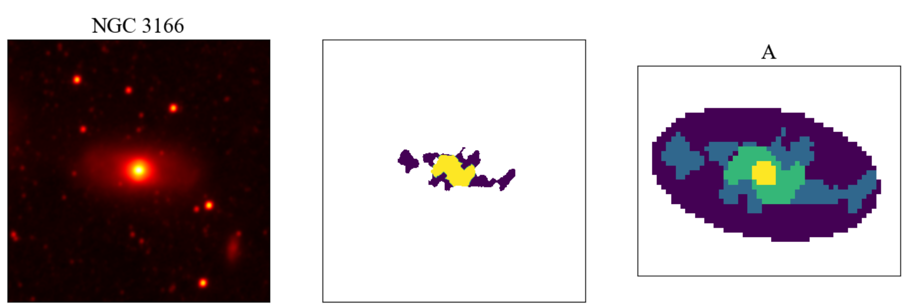

Figure 25: (Continued.)

(22)

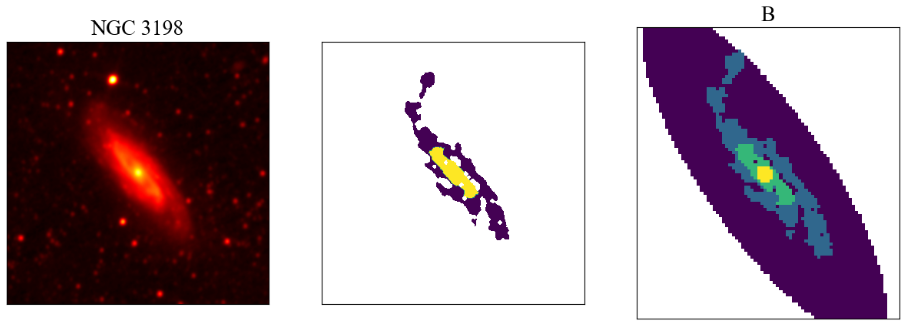

(23)

(24)

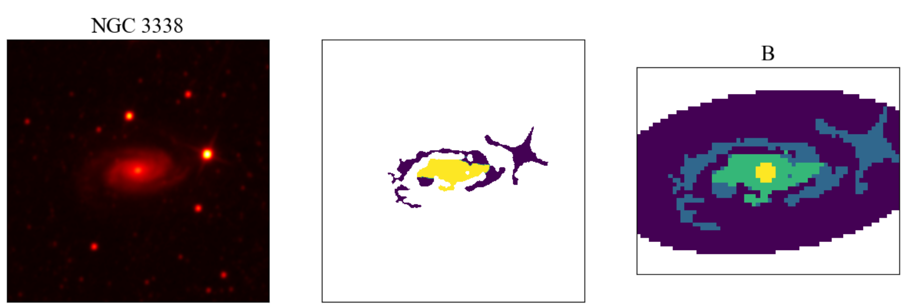

Figure 25: (Continued.)

(25)

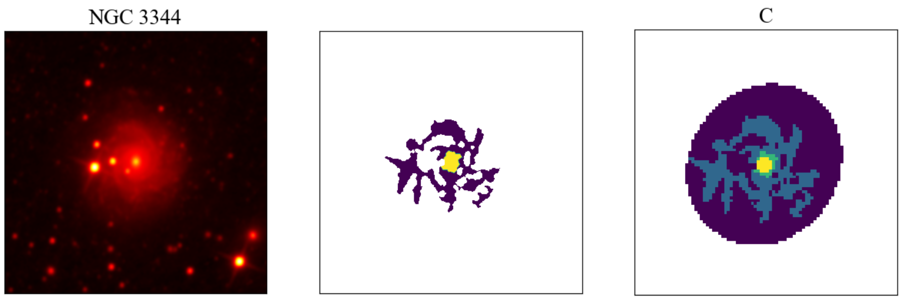

(26)

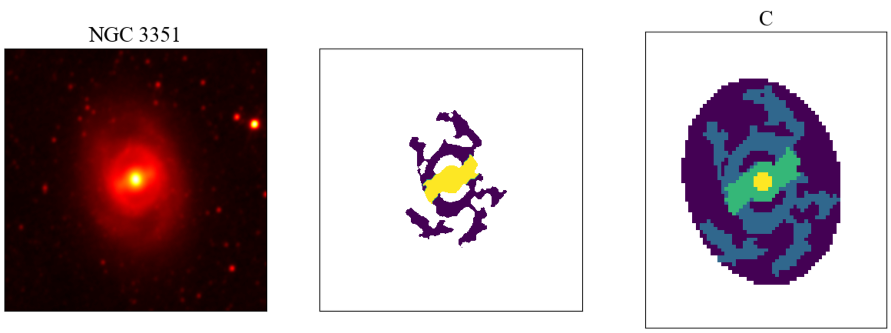

(27)

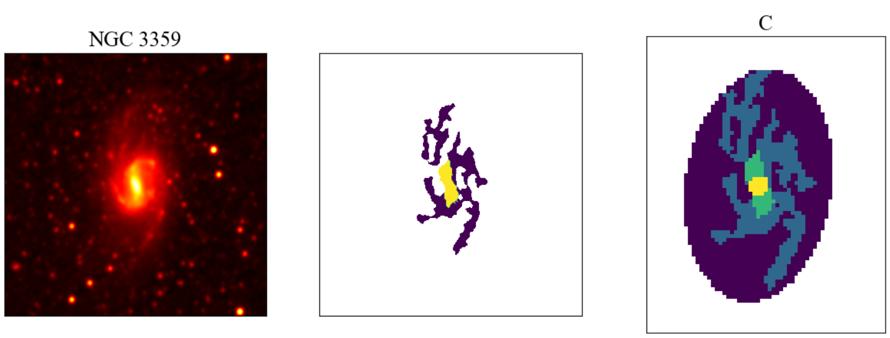

Figure 25: (Continued.)

(28)

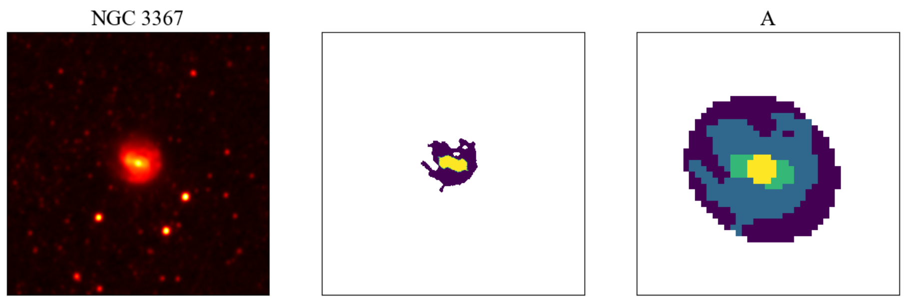

(29)

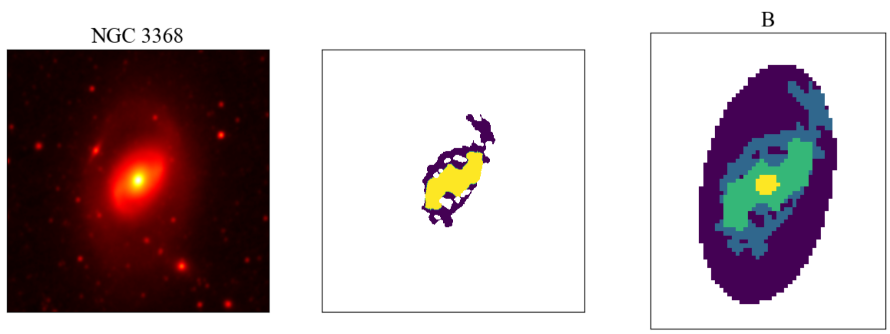

(30)

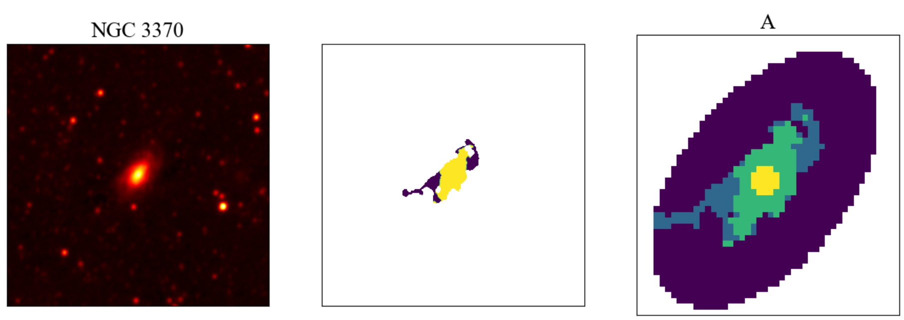

Figure 25: (Continued.)

(31)

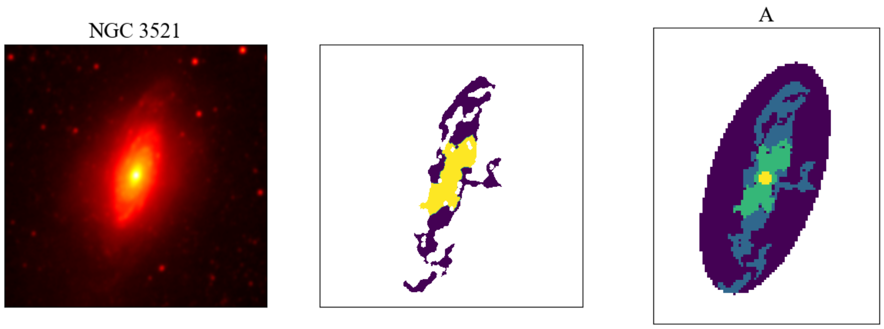

(32)

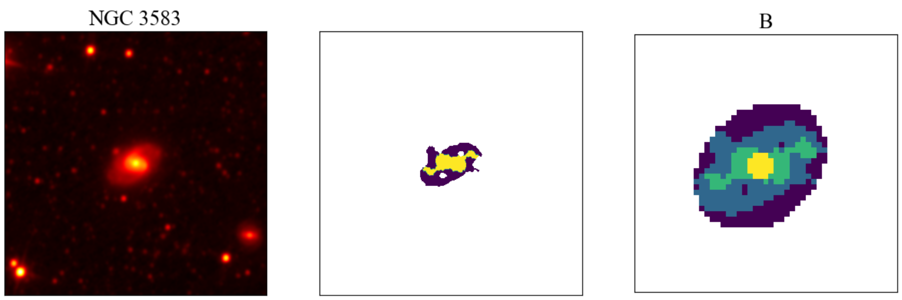

(33)

Figure 25: (Continued.)

(34)

(35)

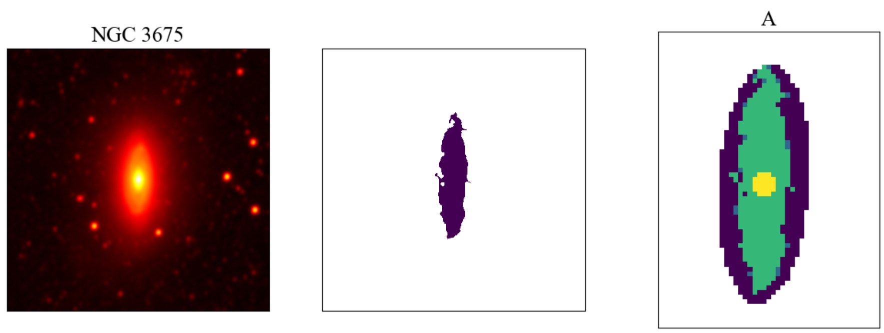

(36)

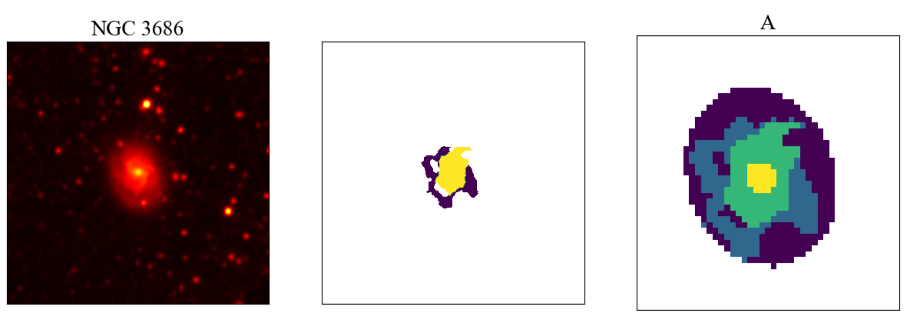

Figure 25: (Continued.)

(37)

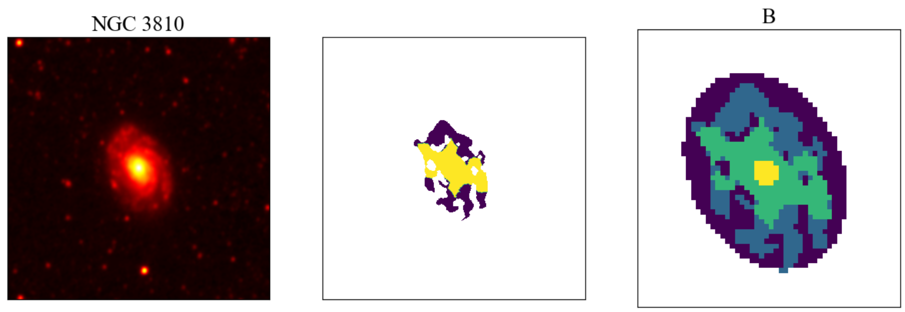

(38)

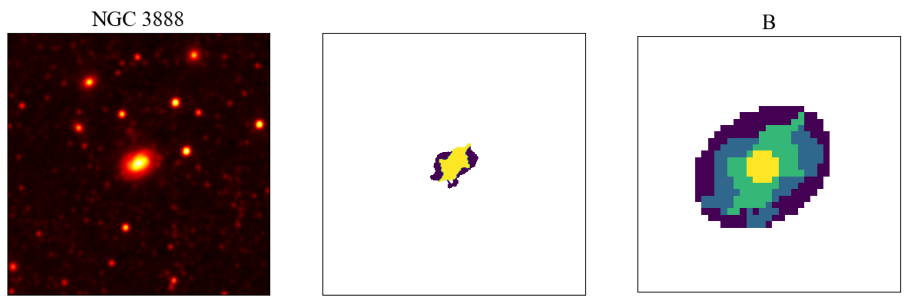

(39)

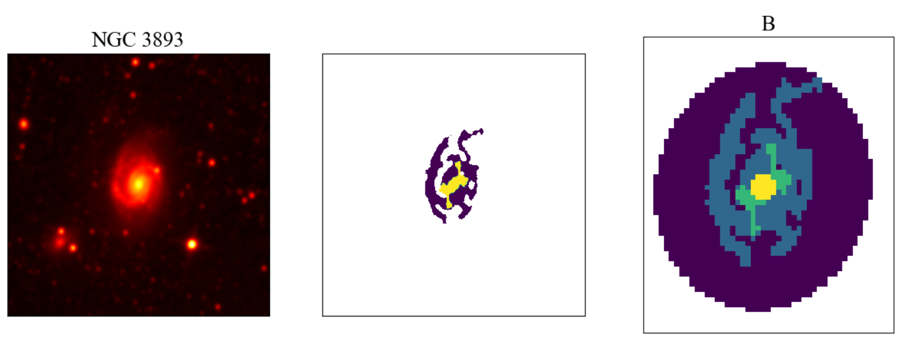

Figure 25: (Continued.)

(40)

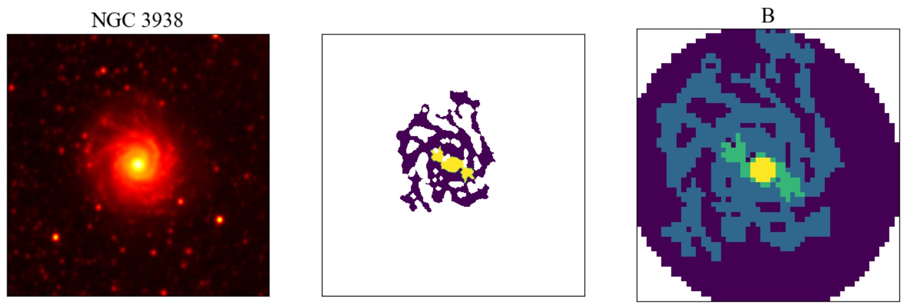

(41)

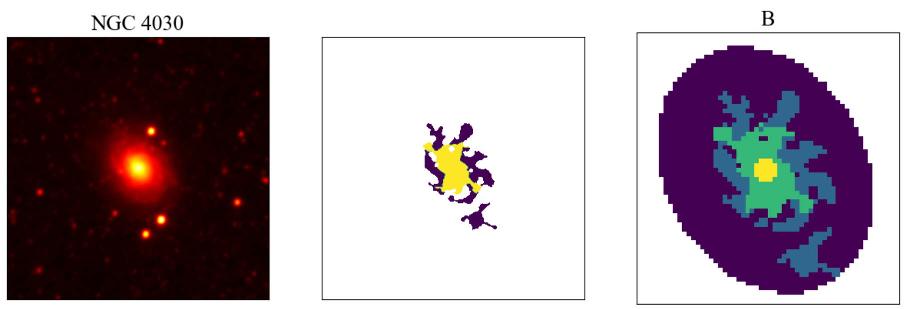

(42)

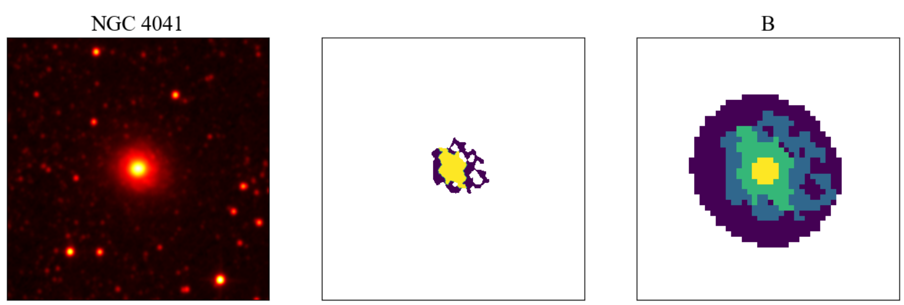

Figure 25: (Continued.)

(43)

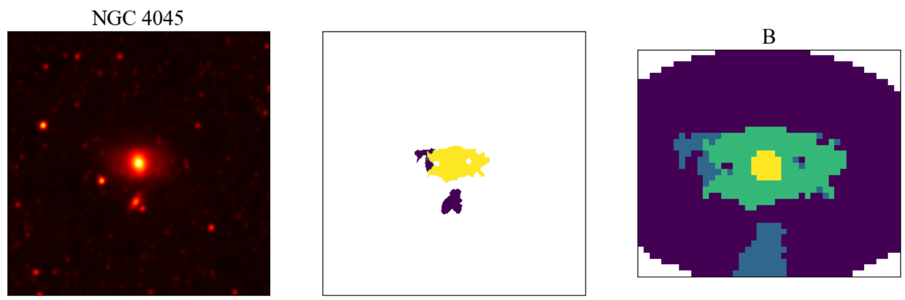

(44)

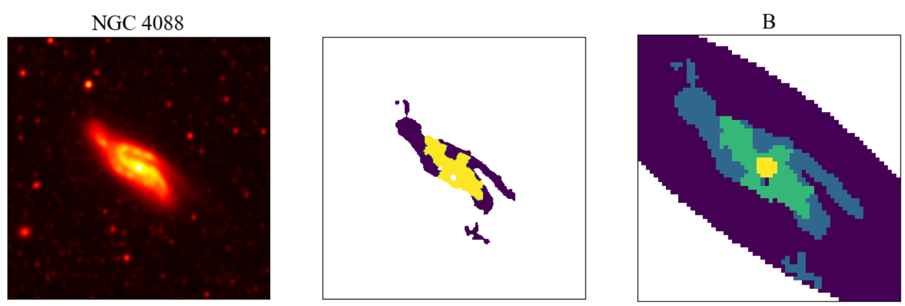

(45)

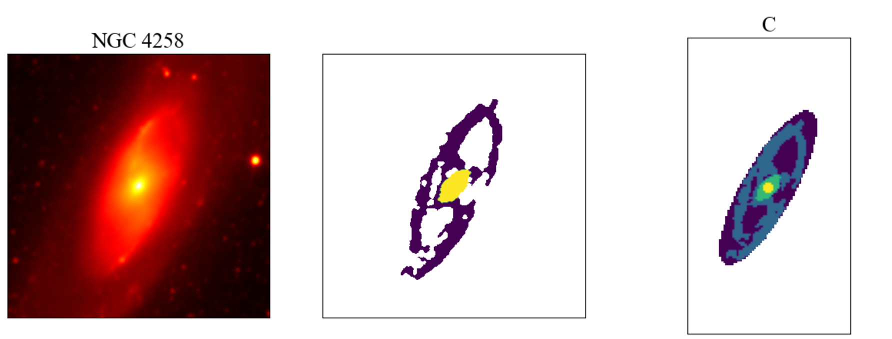

Figure 25: (Continued.)

(46)

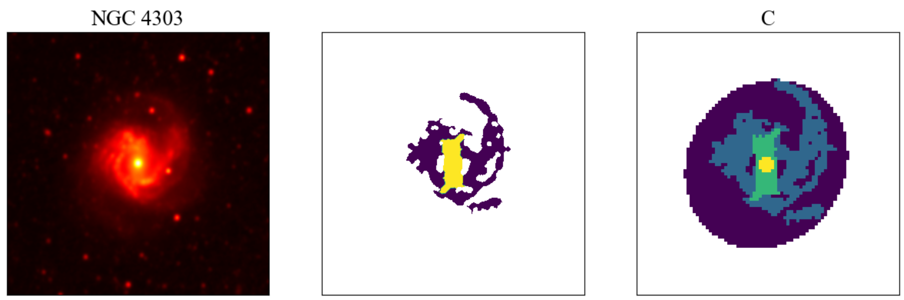

(47)

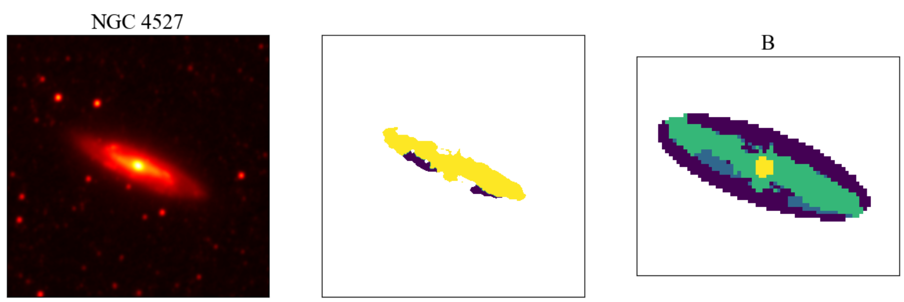

(48)

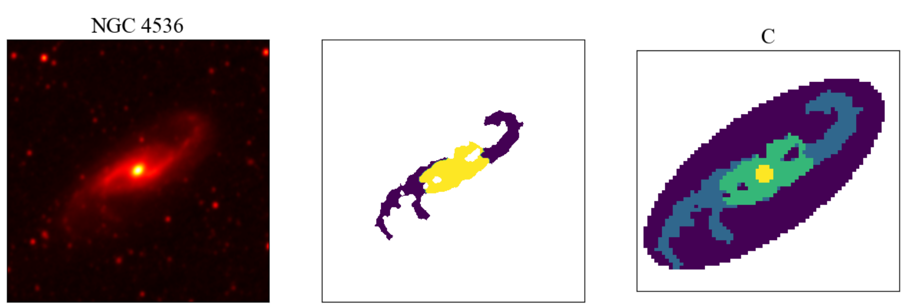

Figure 25: (Continued.)

(49)

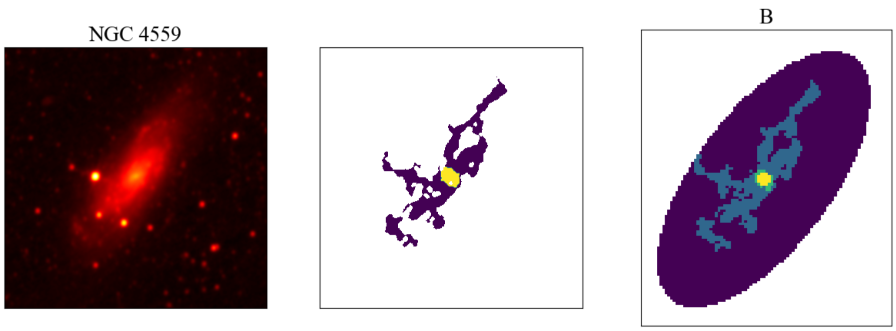

(50)

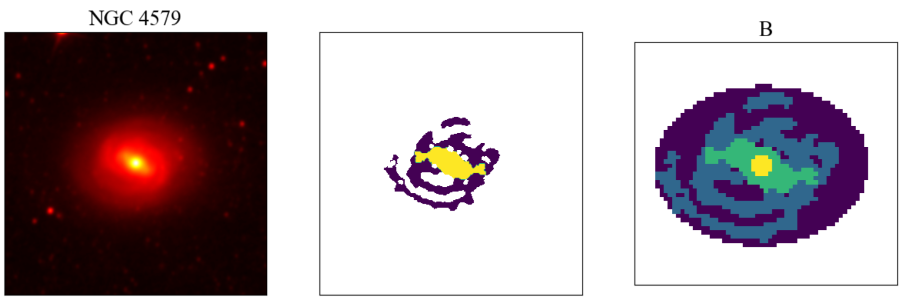

(51)

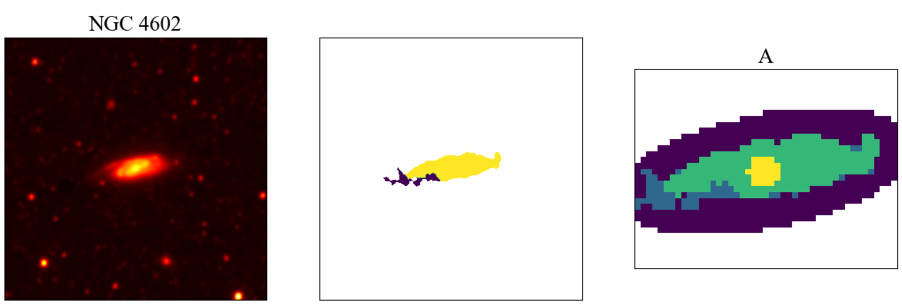

Figure 25: (Continued.)

(52)

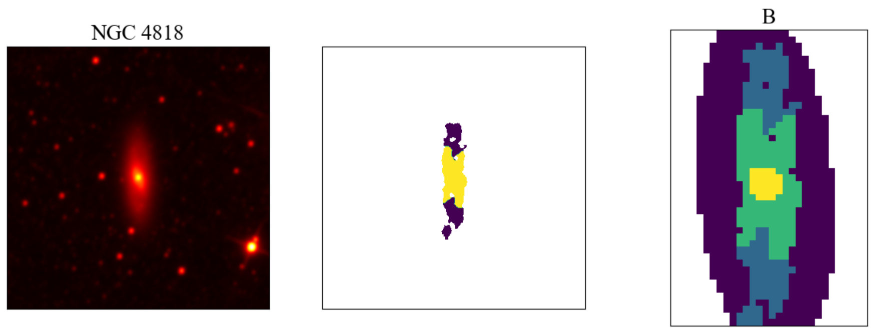

(53)

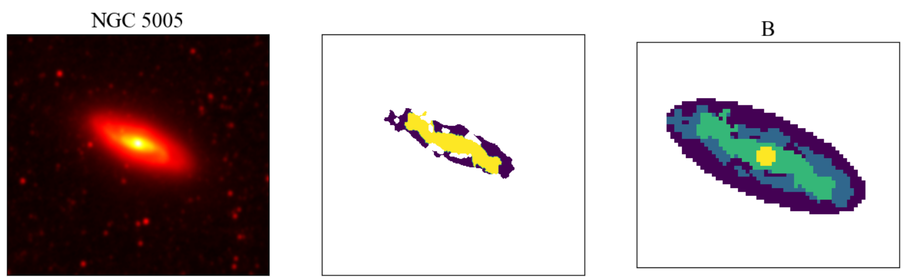

(54)

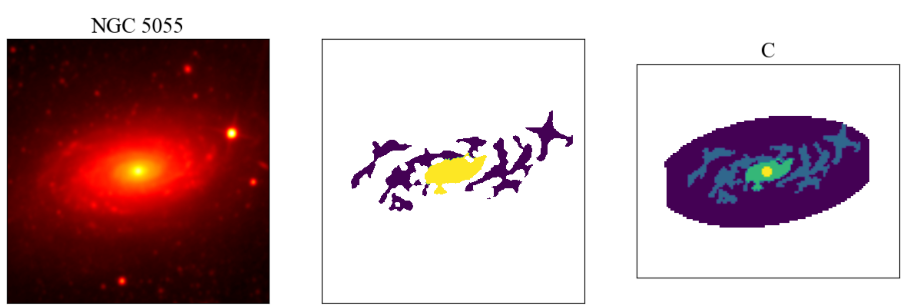

Figure 25: (Continued.)

(55)

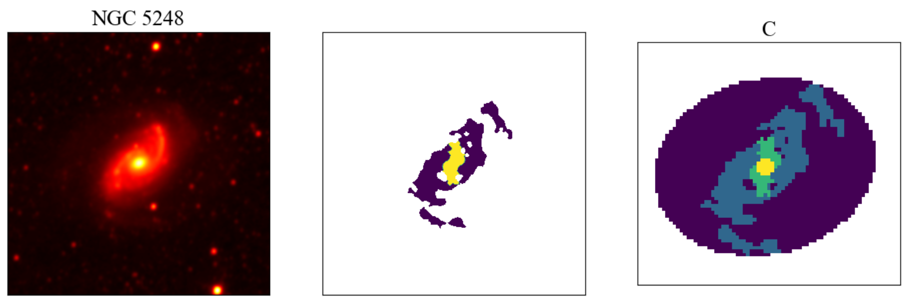

(56)

(57)

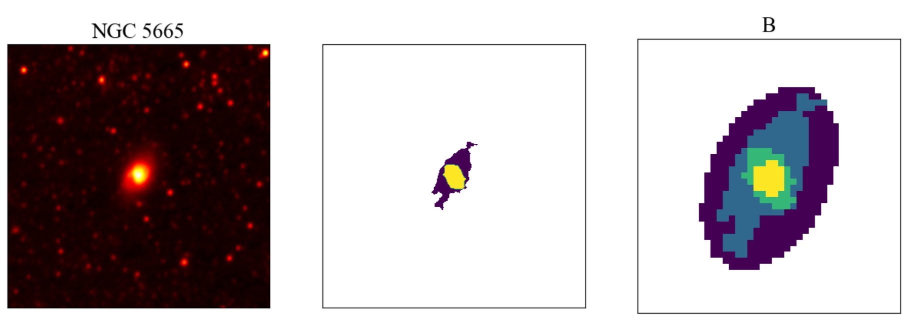

Figure 25: (Continued.)

(58)

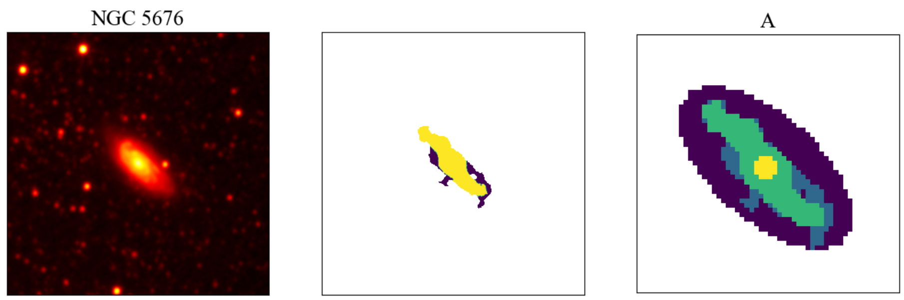

(59)

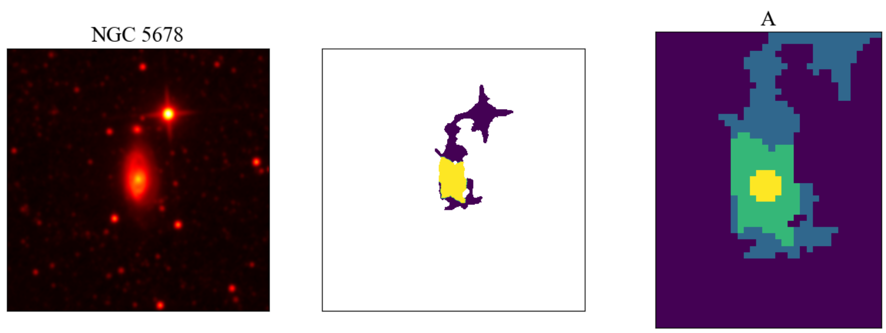

(60)

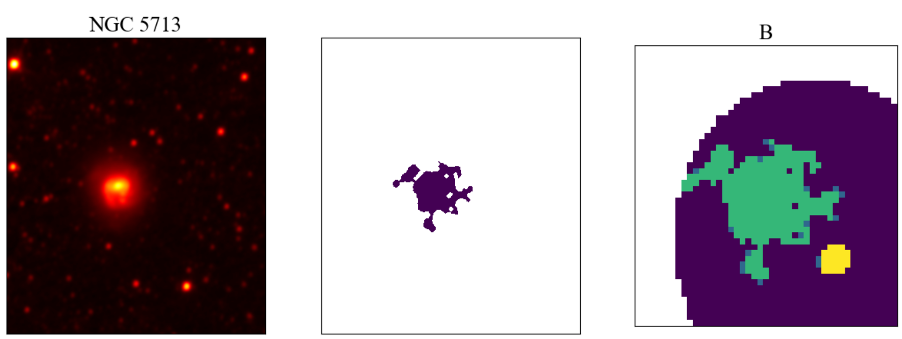

Figure 25: (Continued.)

(61)

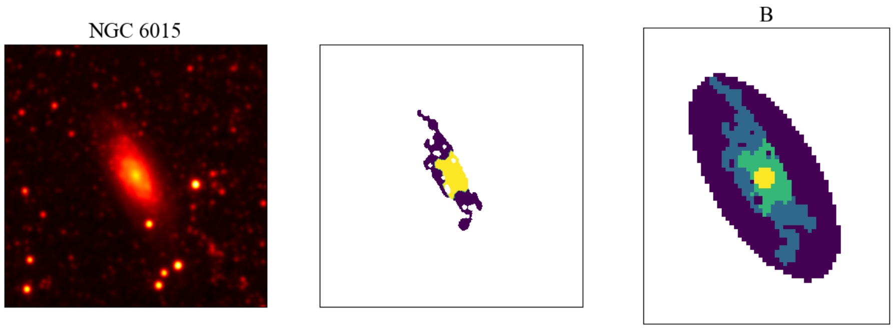

(62)

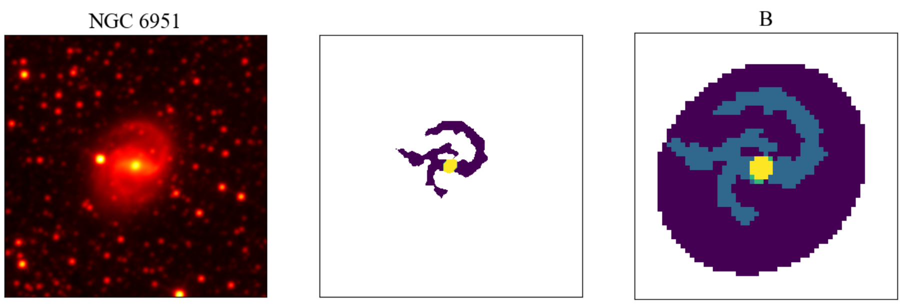

(63)

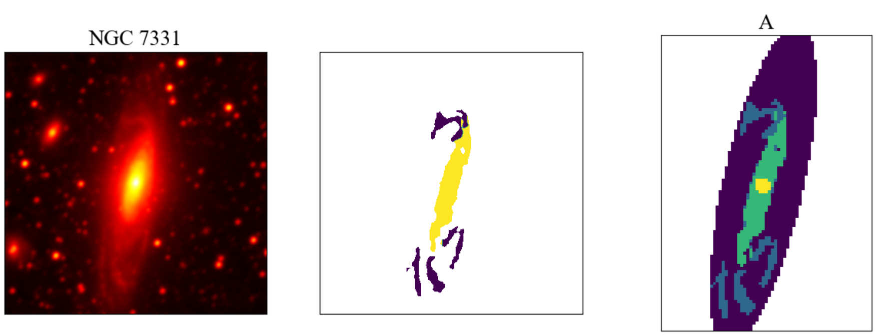

Figure 25: (Continued.)

(64)

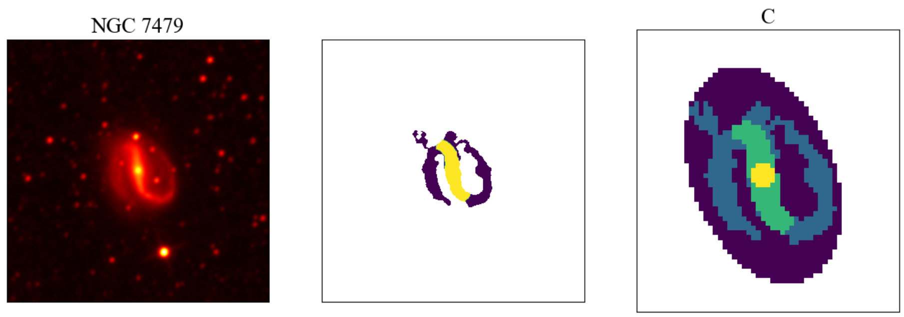

(65)

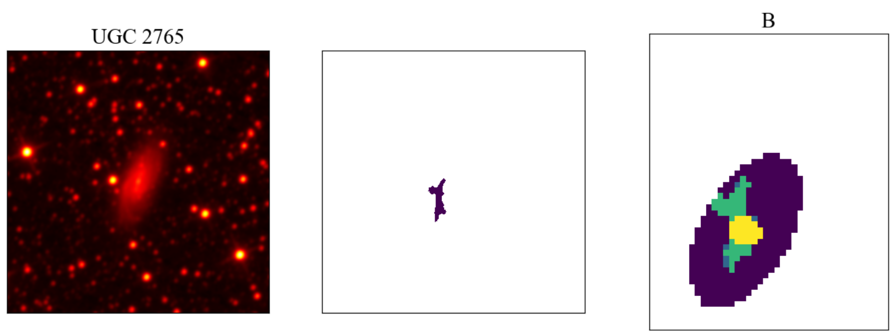

(Continued.)